Implantable Molecular Tracker: Development and commissioning of the electrical system

Master Thesis

In partial fulfillment of the requirements for the degree

"Master of Science in Engineering"

Master program:

Mechatronics & Smart Technologies

Management Center Innsbruck

Supervisor

Stanford University

Prof. Dr. H. Tom Soh

Internal supervisor:

FH-Prof. Bernhard Hollaus, PhD

Author:

Philipp Thoma

2210620022

Declaration in Lieu of Oath

I hereby declare, under oath, that this master thesis has been my independent work and has not been aided with any prohibited means. I declare, to the best of my knowledge and belief, that all passages taken from published and unpublished sources or docments have been reproduced whether as original, slightly changed or in thought, have been mentioned as such at the corresponding places of the thesis, by citation, where the extend of the original quotes is indicated.
The paper has not been submitted for evaluation to another examination authority or has been published in this form or another.

Place, Date

Signature

Acknowledgement

I would like to express my deepest gratitude to my supervisor, FH-Prof. Bernhard Hollaus, PhD, for his invaluable guidance, continuous support and encouragement throughout this research project. His insights and expertise have been instrumental in shaping this work.
I am also deeply thankful to my host professor, Prof. Dr. H. Tom Soh, for welcoming me to his research group and providing me with the resources and opportunities to grow both academically and personally. His mentorship and constructive feedback have greatly enriched my experience. I extend my sincere thanks to the entire Soh lab for their collaboration, support and for creating such a welcoming environment. Their camaraderie, assistance and shared passion for research have made my time with them incredibly rewarding.

I would also like to extend my heartfelt thanks to the Austrian Marshall Plan Foundation for their generous financial support. Their contribution has been essential in making this project possible.

Abstract

Gathering physiological and chemical data inside the human body within minutes is key to improve medical treatments and outcomes. This master's thesis focuses on the hardware development of an implantable medical device that integrates a biosensor to measure uric acid inside the human body. Tight spatial boundary conditions in combination with high power requirements pose the main hardware challenges. An LED, combined with collimation and filter optics, triggers the fluorescent biosensors. Low-power electronic readout circuits inside the device translate the emitted fluorescent light signal into a Bluetooth signal. This is read by an external device, like a smartphone. All electronics and optics are housed in a custom design, 3D printed enclosure and sealed with biocompatible glue. After selecting hardware components and designing the PCBs, the electrical and optical system is optimized, including testing the first prototype design. Extensive testing provides precise information about the possible level of detection of the uric acid, as well as monitors power consumption and battery life. Finally, the devices' electrical characteristic is known and can be used for both in vitro and in vivo tests to characterize the biosensors. In future, implantable medical devices, like this one, will enable the monitoring and control of biomarkers like uric acid more accurately. The developed hardware is compatible with biosensors for other biomarkers, making the system versatile.

Keywords: Micro electronic, implant, biosensors, 3D-print, power optimization

Kurzfassung

Die Messung physiologischer und chemischer Daten im menschlichen Körper innerhalb weniger Minuten ist Elementar wichtig, um medizinische Behandlungen weiter zu verbessern. Diese Masterarbeit konzentriert sich auf die Hardware-Entwicklung eines medizinischen elektischen Implantat, das einen Biosensor zur Messung von Harnsäure im menschlichen Körper integriert. Enge räumliche Randbedingungen in Kombination mit hohen Leistungsanforderungen stellen die größten Herausforderungen auf Hardware-Seite dar. Eine LED, mit nachgeschalteter Kollimations- und Filteroptik regt die fluoreszierenden Biosensoren an. Elektronische Ausleseschaltungen mit geringem Stromverbrauch im Inneren des Geräts übersetzen das emittierte Fluoreszenz-Lichtsignal in ein Bluetooth-Signal. Dieses wird von einem externen Gerät ausgelesen. Nach der Auswahl der Hardwarekomponenten wird das elektrische und optische System getestet und optimiert. Ausführliche Tests liefern anschließend genaue Informationen über die die Sensibilität und Beschränkungen des elektischen Systems. Stromverbrauch und Batterielaufzeit werden ermittelt und schließen die Charakterisierung der Hardware ab. In vitro und in vivo Messungen in Ratten characterisieren anschließend die Biosensoren und tragen zur Entwicklung besserer Biosensoren bei. In Zukunft kann dieser implantierbare medizinische Sensor eine genauere Überwachung und Kontrolle von verschiedenen Biomarkern bieten. Die vielseitige Einsatzmöglichkeit des Implantats wird die Behandlungsmöglichkeiten von Patienten verbessern.

Schlagwörter: Mikroelektronik, Implantat, Biosensor, 3D-Druck, Leistungsoptimierung

Contents

1. Introduction

Biomarkers in the human body are crucial for tracking disease progression and responding to physiological changes [1]. Abnormal uric acid levels, for instance, can indicate gout, kidney stones, and chronic kidney disease [2]. Currently, testing uric acid levels requires a blood sample, with patients needing to fast for four hours before the test [2]. The results, typically available within 24 hours, involve laboratory analysis [3].
Continuous monitoring using an implantable or ingestible sensor simplifies this process, providing real-time measurements that reveal concentration gradients and trace medication effects. Interstitial Fluid (ISF) surrounds tissue cells and contains a biomarker composition similar to blood, making it an accessible medium for monitoring. ISF-based continuous glucose monitors detect less than a 10% absolute relative difference from blood-based glucose meters [4].
Implantable sensors offer medics a extensive view of patient's conditions. While blood samples provide snapshots, implantable devices track biomarkers continuously, showing variations and responses to specific events, leading to more targeted treatments. Designing a reliable, efficient, and biocompatible implant, however, presents significant challenges.
For this project, fluorescent labeled aptamers are utilized as affinity reagents. Aptamers are single-stranded DNA or RNA oligonucleotides that bind to proteins with high specificity [5]. They are preferable due to their high stability, low cost, and high specificity compared to other affinity reagents like antibodies and others. Aptamers can be designed and reproduced to target almost any protein [5].
The aptamers are bound to a 3D-printed scaffold, with packing density being the main size constraint for the device. Using fluorescent labeled aptamers require both excitation source and emission detection. Collimation and focusing lenses enhance the output signal intensity, while optical filters minimize excitation light leakage into the emission band, improving signal to noise ratio at the sensor. The electrical system, which includes a battery, radio, excitation LED, and emission sensor, is essential for the implant's functionality. This integration of optical and electrical components is crucial for reliably monitoring uric acid levels in interstitial fluid.
This project aims to develop a baseline implantable sensor that can be easily adapted for measuring various biomarkers. Once the initial setup is completed, the required LED power for detecting different biomarker concentrations can be recorded. The hardware will then be compatible with aptamers designed for other biomarkers, making the system versatile. Uric acid measurement and the current diameter are just starting points. As technology advances and aptamer packing density increases on the scaffold, the device

size can be reduced, potentially leading to the creation of an ingestible sensor.
This paper reviews current ingestible electric capsules and aptamer switches before detailing our device's specifications, including the electrical system (battery, radio, excitation LED, spectral sensor), optical system (filters, lenses), and enclosure. We outline our approach to integration and realization, followed by the presentation of test results. The paper concludes with a discussion for the sensor technology and presenting the remaining problems alongside the achieved baseline.

2. State of the art

In this chapter, the latest products in the field of ingestible and implantable medical sensors are explored. Current technologies in sensor electronics and the use of aptamers for highly specific biomarker detection is shown. This overview provides the necessary context and highlights the technological foundations that this project is built upon.

2.1. Ingestible electronic capsules

Ingestible pills and implantable sensors share very similar technological challenges, making it relevant to analyze currently available ingestible products to design of a high quality implant.
Existing ingestible electronic pills on the market are designed for measuring body core temperature, detecting fluorescence, or performing video endoscopy. Most pills are used for video endoscopy. Relevant products in this area include Medtronic PillCam SB3 [6], Intro-Medic MiroCam [7], and others such as those by the Jinshan group [8], Olympus [9], CapsoVision [10] and RF SYSTEM lab [11]. Capsules used for infrared fluorescence cancer screening and fluorescence capsule endoscopy are more closely aligned with the concept of the Implantable Molecular Tracker (IMT), though they still utilize different measurement techniques. Both types detect fluorescence optically, but one relies on an externally introduced fluorophore that reacts with tissue [12], while the other utilizes autofluorescent substances like Flavin Adenine Dinucleotide (FAD) [13]. The latter also employs an Application-Specific Integrated Circuit (ASIC) chip, making the design especially compact.

2.2. Implantable sensors

Several continuous glucose monitoring implants are currently available, all of which are powered wirelessly using a separate, rechargeable device placed just above the implanted sensor. One prominent example is the Senseonics Eversense E3, which also uses an ASIC chip to minimize the implant's size [14].
Despite these advancements, there are currently no available implant that measure biomarkers other than glucose in the ISF. In summary, the most promising ingestible pills and implants are characterized by their small size and the use of custom silicon components. However, this makes the development process long and expensive.

2.3. Bio-chemical working principle

The high level working principle of the IMT is as follows: The surface of a 3D-printed scaffold is functionalized with DNA-based aptamer switches. They change their shape upon binding to the target biomarker. Fluorophores bound to the aptamers are thereby activated [15]. The activated fluorophores can then be excited with a LED. Fluorophores absorb light and emit it in a longer wavelength, afterwards. This emission light can be detected. The intensity of the emitted light indicates the amount of activated aptamers. The main challenge is to detect one single biomarker in a solution containing many biomarkers. Many proteins in the body serve as biomarkers. There are three common ways to detect specific proteins:

- Solution-based assays.
- Mass spectrometry.
- X-ray crystallography, NMR, Cryo-EM, circular dichroism [5].

A solution-based assay is used for the IMT system. Usually, three components are necessary for a protein assay: affinity reagent, signal transducer and detector [5]. The affinity reagent binds specifically to the target protein, the transducer converts the binding into a signal, the detector creates an electrical signal out of it. In the IMT, aptamers function as the affinity reagents.
Aptamers are single-stranded DNA or RNA oligonucleotides. They bind to proteins with high specificity [5]. Aptamers are used for the IMT because they are stable, cost-effective and provide high specificity, compared to other affinity reagents like antibodies, molecularly imprinted polymers, protein ligands, lectins, antibody mimetics and enable continuous monitoring through reversible binding. Additionally, they can be designed and reproduced to react with almost any protein [5].
The aptamers are labeled with fluorophores, which act as optical signal transducers. The detector is a light sensor in the electrical system of the IMT that converts the light intensity at the emission wavelength into a digital ADC value.
Thus, the aptamers react with the target biomarker, thereby activating fluorescent labels that quantify the number of reactions happening.

2.3.1. Aptamer

Aptamers are typically created in a process called Systematic Evolution of Ligands by EXponential enrichment (SELEX). This process starts with a large library of DNA or RNA oligonucleotides with random sequences. The target protein is then introduced, allowing some oligonucleotides to bind with high affinity. The sequences that do not bind are washed away. The bound proteins are subsequently removed from the oligonucleotides, which are then amplified for subsequent rounds of selection. This cycle is repeated up to 15 times, with increasing stringency to select for strong binders. Finally, stable, highly specific binding aptamers are created by cloning [5].

2.3.2. Fluorophore

Fluorescent molecules absorb light, which is later emitted at a longer wavelength (reduced energy). The two main characteristics of fluorophores relevant for signal detection are the Stokes shift and quantum yield. The Stokes shift is relevant for the signal separation between absorbed and emitted light, which is crucial for distinguishing the signal from the excitation source. Quantum yield determines the overall brightness of the emissions [5]. Together, these properties influence the minimum detectable concentration of the target biomarker.
The choice of fluorophore and its emission spectrum is based on three criteria:

- LED forward voltage drop
- Cell autofluorescence
- Sensor channel separation.

Red light is of lower energy than shorter wavelengths, resulting in a smaller forward voltage drop for the excitation LED. A green LED was tested to have a forward voltage drop of $2.2\,\mathrm{V}$, while a red LED has $1.8\,\mathrm{V}$. This is significant because, as the battery voltage decreases with its state of charge, sufficient headroom is needed for the LED driver to supply the desired current. This makes red light the superior choice in terms of forward voltage.
Cell autofluorescence is expected to be minimal, but it can be further reduced by selecting an appropriate excitation wavelength. To minimize interference, wavelengths corresponding to dominant autofluorescent emissions should be avoided. Most endogenous fluorophores respond to wavelengths below $600\,\mathrm{nm}$ [16]. Therefore, using red light, above $600\,\mathrm{nm}$, is advantageous for excitation purposes.
The AS7341 light sensor covers 11 separate channels, each detecting different parts of the visible and invisible light spectrum. Tests with green and red excitation light using the fluorophores Cy3 and Cy5, respectively, have demonstrated the benefits of red light in combination with Cy5. Green excitation light affects sensor channels F4 and F5, with the Cy3 emissions impacting F5 and F6. The high excitation intensity makes F5 unusable for signal detection and reduces F6's intensity. In contrast, red LED excitation mainly impacts F7, while Cy5 emissions are detected in F8, with minimal signal in F7.
Considering these three factors, the red light and Cy5 were selected.
There are also other fluorophores in the red spectrum, such as Atto643, which could be considered. Atto643 is approximately $23\,\%$ brighter than Cy5 [17] [18]. However, Cy5 remains the preferred choice for the molecular side of the project because it is easier to attach to the aptamers.

2.4. Electrical

This section first shows different possible energy sources available for the implant. Later, the most pressing information in the wireless data transmission are described.

2.4.1. Energy source

One of the most fundamental components of biomedical electronic devices is the power source. It enables the sensors to gather valuable data. Enhanced battery life results in more analysable data, helping to find relevant patterns or changes quicker and with less effort.
Three different options for supplying electrical power for these devices are available:

- Energy harvesting
- Wireless power transfer
- Batteries

Each biomedical electronic device faces its own set of challenges, favoring one over the others. Energy harvesting captures mechanical, chemical and electromagnetic energies from within the human body. The type and amount of energy that can be harvested depend on the device's location. For example, the best possible mechanical energy harvesting close to the ankle provides up to $66.8\,\mathrm{W}$, while the best chemical energy harvest inside the colon was tested to provide $7.3\,\mu\mathrm{W\,cm^{-2}}$ with an averaging voltage of $308\,\mathrm{mV}$, utilizing a microbial fuel cell [19]. As a result of the position of the IMT in the torso and the lack of sufficient chemical power to supply an optical implant, energy harvesting is not feasible for the IMT.
Energy transfer is also possible in multiple different ways. There is mechanical and electromagnetic energy transfer [19]. However, the IMT's aim to be easily usable without any external accessories, like an ultrasonic transmitter or antenna prohibits energy transfer as a viable option.
This leaves batteries as the best option to power the IMT, as they combine small size and sufficiently high power. Medical devices are heavily regulated. Thus, the general safety requirements for batteries in medical devices are outlined in the IEC 60601-1 standard [19]. Batteries come in many different shapes and with a broad range of chemical compositions, but due to the IMT's cylindrical shape with rounded ends, coin cell batteries are the only option that fits. Pouch or prismatic cells would not fit into the design with tight spacial boundaries.
Zinc-air batteries seem promising initially because they have a high volumetric energy density. However, they are not suitable for the IMT because they require an air supply to work. Theoretical calculations indicate that a zinc-air battery would need approximately $1.2\,\mathrm{dm^3}$ of air per Ah [20]. For a battery capacity of $100\,\mathrm{mA\,h}$, the resulting air volume is unfeasible big for the IMT.
Lithium-ion batteries have high capacity and a low self-discharge rate, but they have big safety issues in case of physical damage, high temperatures, short circuits and overcharging. Additionally, the electrolytes inside are toxic to humans. Failing to properly setup a protection circuit can lead to thermal runaway or explosion of the cells [19].
Lithium-manganese-dioxide cells have a high thermal stability, reducing the risk of thermal runaway. However, they lack the high power output necessary for the IMT [21].

Ultimately, the only viable option for the IMT, as an implantable device, is a silver oxide battery. Despite their low performance compared to the other chemical battery compositions, silver oxide batteries are the only ones approved by regulatory authorities for clinical use, because they are not prone to thermal runaway and can also be easily disposed of [19], [22].

2.4.2. Data transmission

The IMT is supposed to transmit data from inside the human body to the patient's smartphone, allowing for appealing and informative real-time data display. Modern smartphones are equipped with antennas for Near Field Communication (NFC), WiFi, Bluetooth Low Energy (BLE) and Long Term Evolution (LTE), one of which must be selected.
NFC uses a frequency range centering at $13.56\,\mathrm{MHz}$ [23]. Antennas usually have a quarter or half the length of one wave of the signal, resulting in $11.06\,\mathrm{cm}$ or $5.53\,\mathrm{cm}$, respectively. This is too large to fit in the IMT. Although cellular communication uses a similar frequency range to BLE and WiFi, the antennas, combined with their required chips are too big physically to fit in the IMT.
BLE and WiFi use similar frequency bands in the $2.4\,\mathrm{GHz}$ range. Resulting, the antennas have the same physical properties. But power consumption of BLE is lower than that of WiFi. BLE consumes $71\,\mu\mathrm{J}$ per data packet, while WiFi requires at least $84\,\mu\mathrm{J}$ [24]. Given that power is a valuable asset for the IMT, BLE is the best suited communication protocol.
Bluetooth transmission range heavily depends on path loss. According to the Bluetooth website, a signal range of $55\,\mathrm{m}$ to $78\,\mathrm{m}$ outdoors is reduced to $15\,\mathrm{m}$ to $19\,\mathrm{m}$ in office environments [25]. Human tissue can attenuate the signal even more severely [26]. Table 2.1 shows the experimentally determined attenuation rates for different materials that might be present in the signal path of the implanted IMT.

Table 2.1.: Comparison of attenuation of Bluetooth RF signal in multiple media [26].

Medium	Attenuation rate in $\mathrm{dB\,mm^{-1}}$
Meat	0.397
Ballistic gel	0.314
Water	0.287
Fat	0.193

Most modern BLE fifth generation devices have receiver sensitivities in the range of $-103\,\mathrm{dBm}$ [25]. Assuming the implant is implanted in the worst possible position for signal attenuation, such as the abdominal cavity, some assumptions are necessary to estimate maximum signal attenuation:

- Attenuation in the air from the implant to the smartphone in the patient's hand is neglected due to the short distance.
- The smartphone is positioned in front of the patient, at navel height.
- The transmitter power is $0\,\mathrm{dBm}$.
- Transmitter efficiency is $25\,\%$.

As meat (muscle tissue) has the highest attenuation value (see table 2.1), the thickness of the abdominal muscle and organ tissue is assumed to be $100\,\mathrm{mm}$ combined, leading to an attenuation of$39.7\,\mathrm{dB}$. Typically, the total thickness of the three abdominal muscles (obliquus externus abdominis, obliquus internus abdominis and transversus abdominis) is below $35\,\mathrm{mm}$ for the random study participants, leaving enough headroom for organ tissue. [27]. Additionally, an obese patient could have an additional $200\,\mathrm{mm}$ of fat tissue in the signal path. This leads to $38.8\,\mathrm{dB}$ of attenuation. Adding it up leads to an overall attenuation of $78.5\,\mathrm{dB}$, still leaving headroom to the detection threshold of $-103\,\mathrm{dBm}$. These assumptions neglect that for obese patients the best signal path maybe is through the back, as there is usually less fat, compared to the front. Combining transmitter power and efficiency leads to an effective output power of $-6.02\,\mathrm{dBm}$. Subtracting the path losses of $78.5\,\mathrm{dB}$ still leads to a receiver power of $-84.5\,\mathrm{dBm}$ in the worst case described above.

3. Material & Methods

To achieve the overarching goal of building a working optical implant that detects uric acid, several aspects need to be addressed. Figure 3.1 shows all the components integrated into the design. First, the electronics are developed, with a focus on maintainability and debug capability. The next step is to develop and test the firmware. The working electrical system then needs to be united with the optics and everything securely housed in a custom enclosure.
This section will go through the process of each development, focusing on the most important considerations.

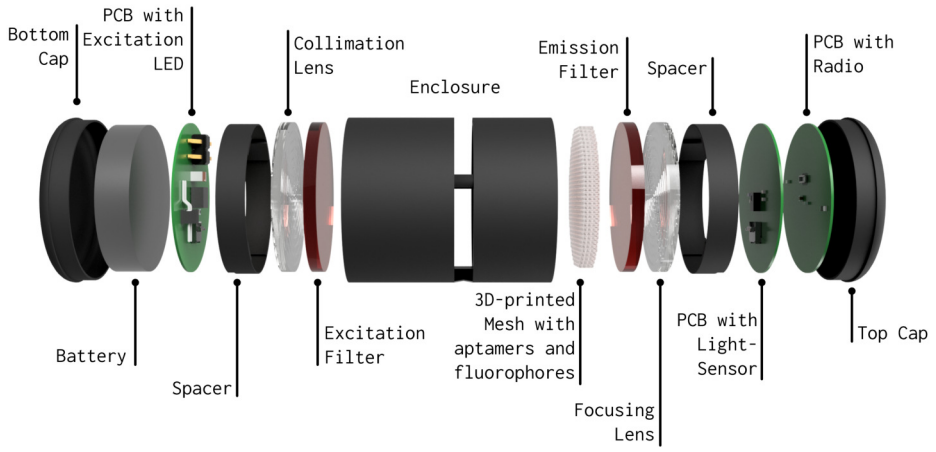

Figure 3.1.: Entire system of the IMT.

3.1. Electrical

The following section will emphasize the part selection and design considerations of the Printed Circuit Board (PCB)s, developed for the electrical system of the IMT.

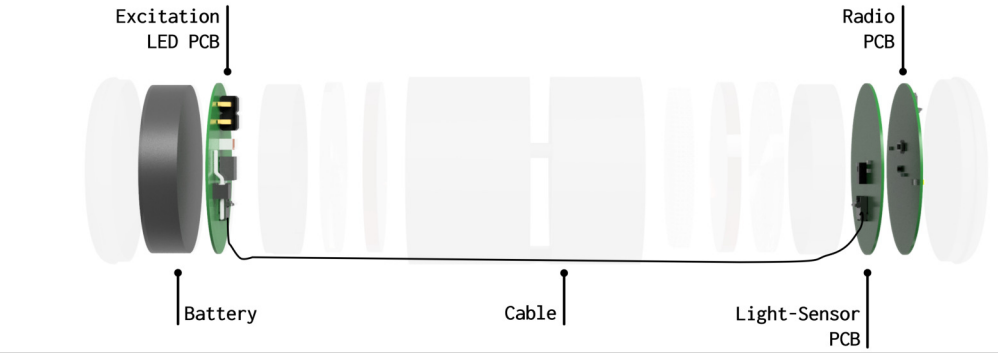

Figure 3.2.: Electrical system inside the IMT.

3.1.1. Components

Microcontroller unit

The selection of a Microcontroller Unit (MCU) is essential for Bluetooth communication and triggering measurements inside the implant. A chip from *Nordic Semiconductor Inc.* was recommended due to its widespread industry use, which ensures strong support and short development times. To accelerate the initial prototypes development, a module that includes a *Nordic* chip, matched antenna, and necessary peripheral components from *Insight SiP* is ideal. Their latest BLE product, the ISP2053-AX, uses the *Nordic* nRF5340 chip.
Given that components in the IMT require different voltage levels, a DC-DC converter is necessary. Although *Nordic* chips in the all ISP modules from *Insight SiP* include a configurable DC-DC converter, older models like the ISP1807-LR do not have accessible pins for this feature. This makes the ISP2053-AX the more favorable option. Additionally, the ISP2053-AX offers lower power consumption compared to the ISP1807-LR, as shown in table 3.1.
While both modules provide more computing power and auxiliary functions than required for the IMT, the lower power consumption and relatively easy implementation of the ISP2053-AX outweigh these considerations. The module, visible in figure 3.3, is compact with a square form factor measuring $8\,\mathrm{mm}$ per side and all pins on the bottom side.

Table 3.1.: Comparison of current consumption of different MCU modules [28] [29].

	ISP2053	ISP 1807
Peak Current, Transmitter $0\,\mathrm{dBm}$	$4.1\,\mathrm{mA}$	$6.4\,\mathrm{mA}$
Peak Current, Receiver 1 Mbps	$3.7\,\mathrm{mA}$	$6.26\,\mathrm{mA}$

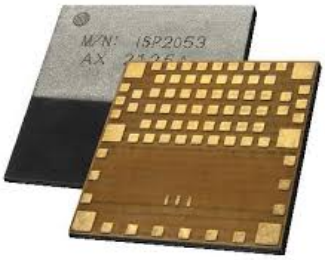

Figure 3.3.: ISP2053 module, integrating the *Nordic* nrf5340 chip [28].

Battery

As mentioned in chapter 2, powering the electrical system is a challenge. While silver-oxide batteries are the only approved option, their electrical characteristics are not well suited for this application. The IMT requires $3\,\mathrm{V}$ and big LED-driving currents (approximately $50\,\mathrm{mA}$) to measure realistic concentrations and variations of uric acid in the ISF. This would necessitate two silver-oxide batteries in series connection, each providing $1.55\,\mathrm{V}$. For the first prototype, silver-oxide batteries do not provide sufficient capacity to endure the high current pulses for the required time of $8\,\mathrm{h}$. As a result, the prototype will use a different battery type.
Ideally, optimizations in the overall system lead to lower noise and thereby power consumption, enabling the use of silver-oxide batteries. o get a proof-of-concept, for the functionality of the IMT, a lithium-ion coin cell battery will be used. This enables to test the IMT with different LED driving currents, while maintaining sufficient battery life.
Therefore, a rechargeable LIR2032 coin cell battery with $3.7\,\mathrm{V}$ nominal cell voltage and a $70\,\mathrm{mA\,h}$ capacity is used in the prototype.

Light source

The goal is to achieve a narrow band, high intensity excitation light beam. There are two main approaches to achieve that:

- Use a LED combined with an optical excitation filter to narrow the band.
- Use a narrow band laser for excitation.

Both alternatives are regulated by the FDA, European union and international standards such as IEC and ISO for medical devices. However, lasers in medical devices have additional regulations, like the *IEC 60825-1 Safety of laser products*, which adds complexity in terms of ensuring and providing compliance. Furthermore, there are no suitable laser products on the marked that meet the spatial constraints of the IMT. Therefore, the decision was made to use a LED and excitation filter.

Preliminary experiments identified the *Luminus* SST-10-R red LED, visible in figure 3.4, as the most suitable light source. In these tests, the light emission power for different LED and collimation lens pairs was measured for a constant LED current of $20\,\mathrm{mA}$. The tests included ultra violet, green and red LEDs, designed for low and high power, from three manufacturers: *Osram*, *Luminus*, and *Rohm Semiconductor*. The main difference between low and high power LEDs is the illuminated surface area and the ability to use higher currents, resulting in brighter light. Both a bigger illuminated surface and higher currents are advantageous for the IMT, favoring the use of a high power LED.
The red LED achieved the highest output power across different collimating lenses. Additionally, red light is advantageous due to lower auto fluorescence of cells in human body at wavelengths above $600\,\mathrm{nm}$, as mentioned in 2.3.2. This makes the red LED an ideal choice. The high power *Luminus* SST-10-R is available in two light emission angles: $90°$ (model -B90) and $130°$ (model -B130). Choosing the $130°$ version saves about $5\,\mathrm{mm}$ in length, to illuminate the whole $25\,\mathrm{mm}$ diameter surface, thereby decreasing the overall implant size. However, the light distribution is not uniform. The center of the illuminated area receives higher light power densities than the outer parts, as seen in the datasheet [30].

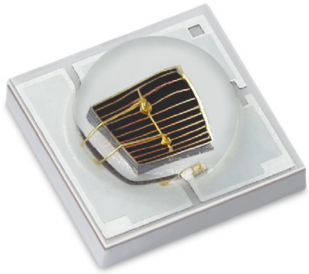

Figure 3.4.: *Luminus* SST-10-R LED. [30]

Sensor

The selection of a suitable sensor is critical for distinguishing between two closely spaced wavelength bands - excitation and emission. Optical filters reduce excitation wavelength leakage to the sensor, but they cannot completely block it, especially when light hits the filters at angles greater than $5°$, as stated in the filter datasheets [31] [32]. This leads to some signal leakage in the excitation band, making it relevant for the sensor to differentiate between excitation and emission light, with the latter being the relevant signal. Using the fluorophore Cy5, these bands are separated by $16\,\mathrm{nm}$, necessitating precise differentiation by the sensor [17]. This is challenging because the emission signal is weak and can easily be masked by excitation leakage.
Single photodiodes typically have too broad a sensitive spectrum, making it impossible to distinguish between the excitation and emission bands. Initial tests identified the *ams OSRAM* AS7341 sensor ass the most suited option. The AS7341 features 11 channels for different wavelengths, each with full width half maximum values between

$26\,\mathrm{nm}$ and $52\,\mathrm{nm}$, including two channels dedicated to the excitation and emission bands. The sensor communicates via I2C and includes a build-in LED driver to control the excitation LED [33]. Figure 3.5 shows the spectrum of each channel of the AS7341 sensor. For use with Cy5, channels F7 (excitation) and F8 (emission) are relevant for the IMT. Notably, channel F8 has the highest spectral sensitivity among the narrow band channels (F1 through F8). This enhances signal detecting and allows for lower uric acid concentration measurement.
The AS7341 needs a $1.8\,\mathrm{V}$ supply and consumes $0.7\,\mu\mathrm{A}$ in sleep mode, reaching up to $210\,\mu\mathrm{A}$ in active mode [33].

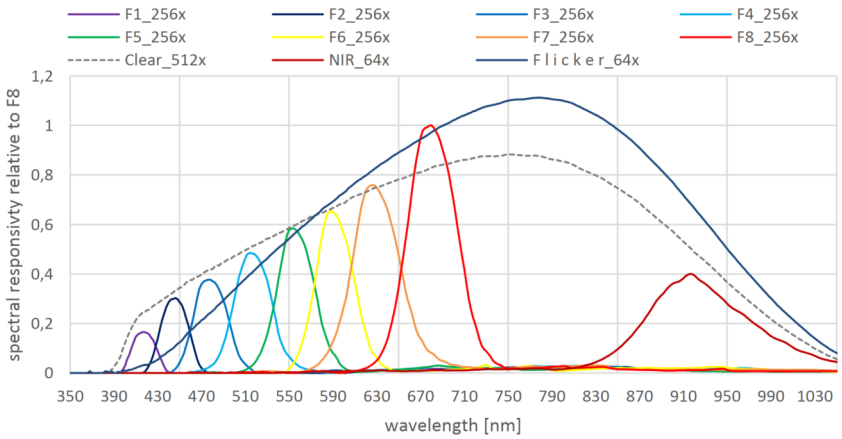

Figure 3.5.: *ams OSRAM* AS7341 sensor spectrum [33].

3.1.2. PCB design

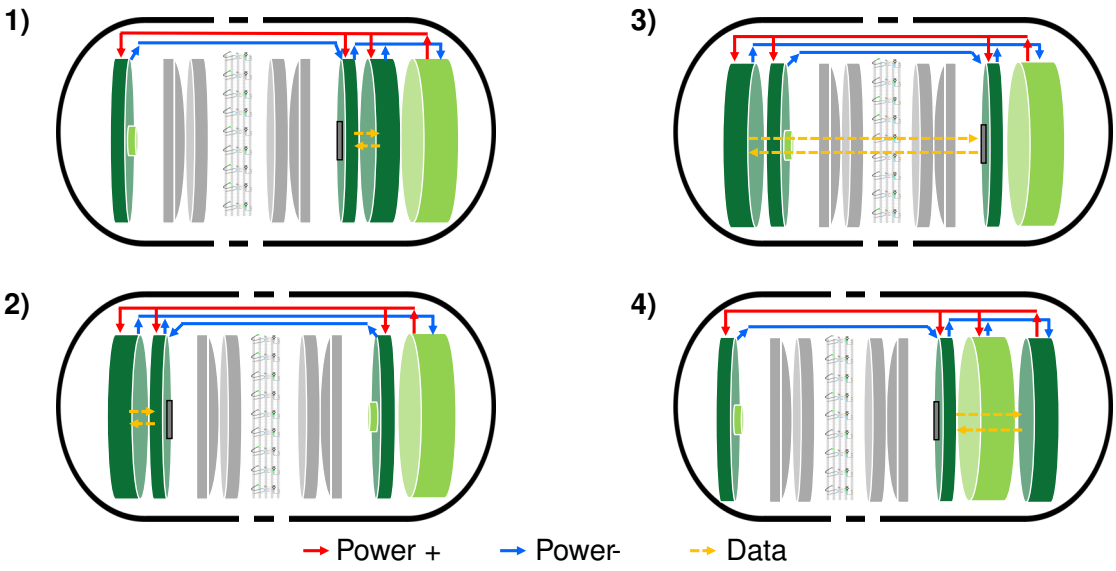

Figure 3.6.: Different arrangements of the PCBs inside the implant.

The layout of the electronics inside the IMT was the result of careful consideration. Four possible configurations for aligning the components were considered, visible in figure

3.6. In the schematic all electronics are colored, while the optical parts are in greyscale. Power and data connections are marked with the three different colored cables. For option 1) in figure 3.6, the electronics from left to right are: LED PCB, sensor PCB, radio PCB and battery. The main constraint arranging the PCBs is that LED and Sensor PCB have to be on opposite sides of optics and sample, facing each other. The arrangement of the PCBs and the battery was varied to find the best design.
In option 3), sensor and radio are too far apart, creating unnecessarily long data transmission cables. Option 4) is overly complex, with PCBs on both sides of the battery, necessitating additional connectors and wiring. In option 1), the radio is sandwiched between the sensor and battery, maximizing metal package around it and potentially blocking the radio signal. Option 2) provides open space for the radio signal to propagate and features relatively simple wiring, making it the most suitable choice.
The following sections will examine the design of each individual PCB. All PCBs have a matte black finish reducing potential light reflections and improving signal quality. They have two layers and are $0.6\,\mathrm{mm}$ thick.

Radio PCB

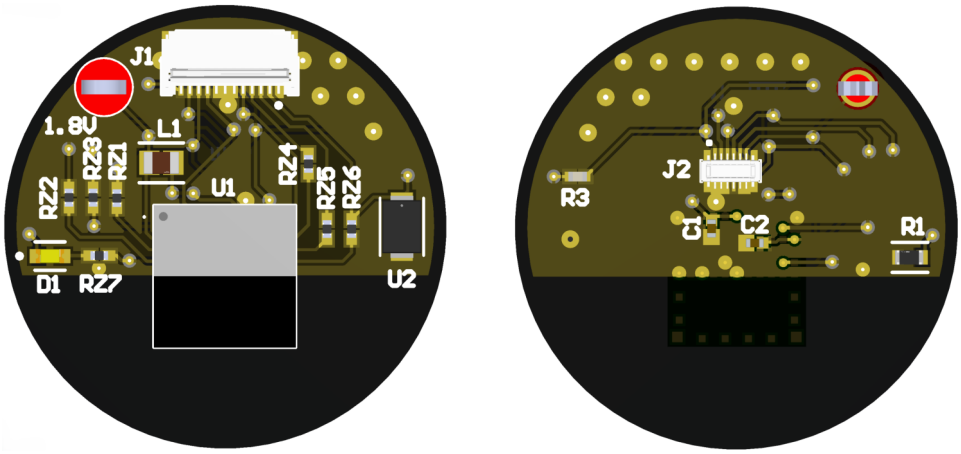

(a) Radio PCB top side

(b) Radio PCB bottom side

Figure 3.7.: Radio PCB

This section focuses on the development of the radio PCB, depicted in figure 3.7. Figure A.1 and figure A.2 in appendix A show the schematics for the PCB.
The key component of this design is the ISP2053 radio module, which is positioned slightly below the middle of the PCB. This position allows for easy adjustments to the PCB diameter, without the need to move multiple components, although it does increase the keep-out area. According to the ISP2053 datasheet, there should be no copper within $1\,\mathrm{mm}$ of the PCB edges, and $5\,\mathrm{mm}$ if no edge is present [28]. This keep-out region starts on the lower half of the module, indicated by the black section visible in figure 3.7a. The slightly darker color of this PCB area compared to the upper parts also indicates the abcence of a copper plane.

The emission light sensor AS7341 requires a $1.8\,\mathrm{V}$supply and the ISP2053 includes a build-in DCDC converter with configurable modes. The appropriate standard circuit configuration, can be found in the nRF5340 datasheet, the base chip of the ISP2053, where several configurations are detailed. Configuration no. 1 is used for this project, It includes battery supply to the *VDDH* pin and enables all DCDC features [34]. By comparing the schematics of the ISP2053 and the nRF5340 chip, the required components to operate the ISP2053 correctly were identified, while avoiding redundancy. Components C1, C2 and L1 in figure A.1 were selected accordingly, with all other components on this schematic sheet added for debugging purposes.
TP1 is a test point, allowing for a connection to a multi meter to measure the output voltage before connecting the sensor PCB, which could potentially cause damage.
Pins F7 and F8 (*OUT_ANT* and *OUT_MOD*) of the module must be connected for normal antenna operation, and seven additional pins (A1, A11, E7, F1, F6, F9, F11) need to be grounded [28].
All signals connected to General-Purpose Input/Output (GPIO) pins on the ISP2053 have $0\,\Omega$ resistors of 0402 size. This setup allows for quick voltage level measurement and, signal disabling by removing the resistor, if necessary. The debug LED (D1) is connected through a current limiting $200\,\Omega$ resistor (R1). It can be configured in the firmware to make it indicate certain events. A reset button with a pull-up resistor is also included for quickly restarting the program during the firmware development.
Figure 3.7 shows both connectors, J1 and J2, located on opposite sides of the PCB. J1 is a 12 pin FPC connector which is as tall as the radio module, with a height of $1\,\mathrm{mm}$ and a signal line pitch of $0.5\,\mathrm{mm}$, making it only $7.7\,\mathrm{mm}$ wide [35]. It connects to the debug PCB and handles power, flashing and the two Inter-Integrated Circuit (I2C) lines. J2 is a 12 pin *molex*, type 505070 connector on the bottom side of the PCB, shown in figure 3.7b. It connects the sensor and radio PCBs, chosen for its low height of $0.6\,\mathrm{mm}$ in mated condition [36], saving space in the overall stack-up. J2 is connected to power and all logic lines from the light sensor (I2C, interrupt, LED driver and GPIO). Only the I2C lines are used in the final firmware, but including all signals in the first prototype is prudent in case they are needed later.
With the ISP2053 having only pins on the bottom side, vias are required for signal access. The combination of the keep-out area and large connector footprints poses a routing challenge to maintain two layers, but saves thickness and production costs, compared to a four-layer PCB. The pin pads of the ISP2053 are too close to place vias next to them, so vias are positioned directly on the pads, necessitating type7 - filled and capped vias. These vias are filled and capped with copper, allowing direct soldering on top of it.

Sensor PCB

The sensor PCB is depicted in figure 3.8. Figure A.3 in appendix A shows the schematic of the PCB.

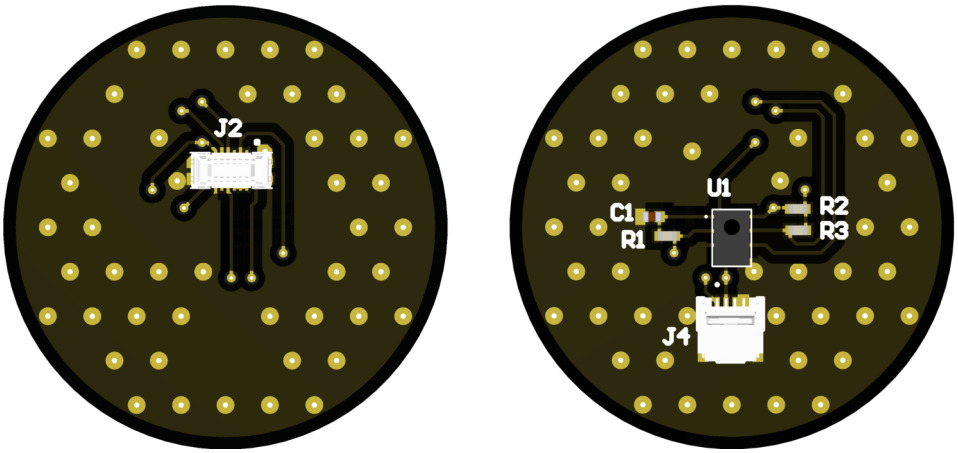

(a) Sensor PCB top side (b) Sensor PCB bottom side

Figure 3.8.: Sensor PCB

The top copper features the female *molex* 505066 series connector that connects to the radio PCB. The bottom copper includes the AS7341 sensor along with its recommended peripheral parts and a 4 pin FPC connector that links to the LED PCB. The AS7341 sensor is placed such that the $0.9\,\mathrm{mm}$ diameter active area is centered on the PCB. The 4 pin connector is positioned as close to the sensor as possible to allow sufficient space for the cables bending radius. This connector includes the LED driver line, battery supply and ground. The battery VCC is only transmitted through the sensor PCB to power the radio PCB. The radio PCB then provides the $1.8\,\mathrm{V}$ supply for the sensor.
All three resistors are $10\,\mathrm{k\Omega}$ pull-up resistors. They are connected to the two I2C lines and the sensors interrupt pin. Additionally, capacitor C1 is added as a filter to address potential voltage ripples. Both the pull-up resistors and the filtering capacitor are recommended in the AS7341 datasheet [33].
To enhance the design, automatic via stitching was added, connecting top and bottom copper ground planes. This improves ground return paths, enhances heat dissipation and reduces noise [37].

LED PCB

The LED PCB is depicted in figure 3.9. Figure A.4 in appendix A shows the schematic of the PCB.
The PCB's bottom side has no components, see figure 3.9b. A battery holder, type BH-125A-1, is soldered there, instead of the BC2032-E2 depicted in the schematic, due to space constraints. Except for the two holes for the battery holder, all vias are for ground stitching.
Connector J3 on top copper, see figure 3.9a, allows easy connection to an external voltage source during firmware development and testing. Connector J2 enables a quick circuit break between the battery and the rest of the system by disconnecting the positive pin of the battery. If there is a battery and an external voltage source connected, the

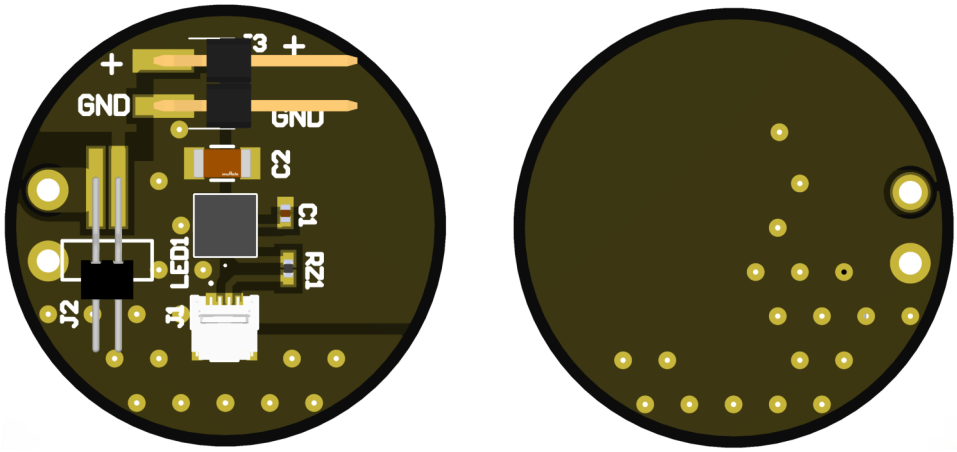

(a) LED PCB top side

(b) LED PCB bottom side

Figure 3.9.: LED PCB

battery is not needed and can easily be disconnected without actually taking it out of the battery holder.

Capacitor C2 is a $100\,\mu\mathrm{F}$ buffer capacitor, stabilizing the supply voltage on all PCBs. Like all the Integrated Circuit (IC)s, the LED also has its own additional $1\,\mu\mathrm{F}$ filter capacitor. The LED is directly connected to the supply voltage. The LED's ground line is the signal line connected to the LED current driver on the sensor PCB, via connector J1. The pinout of the J1 connector is mirrored to match the sensor PCB, since the PCBs face each other in the assembly.

Although, there is no dedicated battery protection circuit to prevent deep discharges, some level of protection is achieved through the component characteristics. The LED, when turned on, is the main current consumer in the electrical system, with standby current around $500\,\mu\mathrm{A}$ and LED current typically set to $37\,\mathrm{mA}$. When the LED is activated, the battery voltage can drop by up to $0.1\,\mathrm{V}$ and then recover once the LED is off. When the battery is close to being discharged, its voltage drops from about $3.6\,\mathrm{V}$ to below $2\,\mathrm{V}$, which is insufficient to power the LED, effectively turning off the main current consumer.This is observed in the measurement data as a reading of *0*, indicating the absence of excitation light. The remaining current is low enough for recharging the battery within a reasonable time frame, avoiding discharges below $1.8\,\mathrm{V}$.

Debug PCB

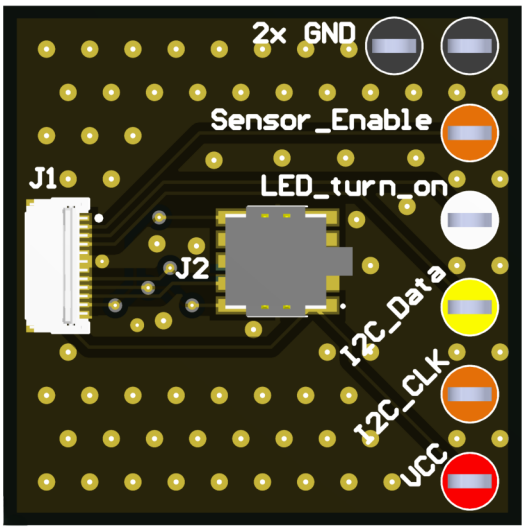

Figure 3.10.: Debug PCB

The debug PCB is shown in figure 3.10, with its schematic detailed in figure A.5 in appendix A.
The main functionality on this PCB is connector J2, which is a ten pin connector for a SEGGER J-link debugger. This connector follows the standard pinout, requiring the SWDIO, SWDCLK and Reset pins of the target microcontroller to be connected. Connector J1 connects to J1 on the radio PCB. Like for the LED and sensor PCBs, the pinouts need to be mirrored.
Additionally, the debug PCB includes measurement probe hooks for easy acces to the most relevant signals. The entire electrical system can also be powered through the *GND* and *VCC* pins on the debug board.

3.2. Software

Software development started after the PCBs were ordered. Initially, a development kit with the ISP2053 and the AS7341 Evaluation Kit were used to implement basic functionality. The software was developed in smaller parts, starting with the I2C implementation to perform basic operations. Then, Bluetooth was implemented and the data transmission manipulated. Finally, I2C and Bluetooth were integrated and the complete firmware was tested as a single unit.
This section will guide through the development process of the firmware.

3.2.1. Development environment

Nordic Semiconductor provides the *nRF Connect* Software Development Kit (SDK), which is fully integrated into the Visual Studio Code environment. There are numerous fully working examples available for testing on development boards, including one specifically for the ISP2053 module. The development boards for the nRF5340 and ISP2053 are mostly interchangeable, only few pins are wired differently. Once adapted to the differences, the ISP2053 development board works seamlessly with the examples provided by *Nordic*, which drastically improves the development speed.
Bluetooth functionality can be easily tested using the *nRF Connect* Desktop app, or the mobile versions available for Android and IOS. These apps show all relevant data clearly and are user-friendly.

3.2.2. I2C

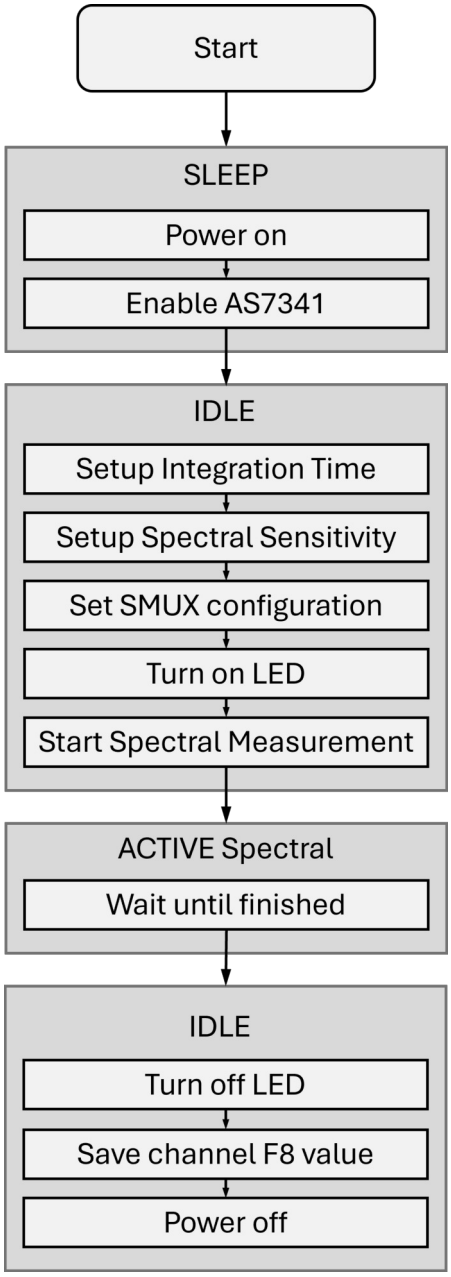

Figure 3.11.: I2C measurement cycle.

I2C is a commonly used protocol for digital communication between ICs. It is a two-wire system for bidirectional data transfer between master and slave devices. One wire is the Serial Data Line (SDA), the other the Serial Clock Line (SCL). The upper limit for number of connected devices at the bus is given by the maximum bus capacitance of $400\,\mathrm{pF}$ and the address space [38].
For the IMT, I2C is practical since both the ISP2053 radio module and the AS7341 light sensor feature I2C interfaces. The AS7341 sensor has the I2C address $0x39$ [33].
The AS7341 Evaluation Kit was used to develop the necessary I2C protocol, allowing for setting up and starting measurements. The kit comes with a software, *AS7341 Demo*

ALS, that can trigger measurements from a connected computer. Initially, the I2C code was developed using the sensor's datasheet and comparing it to the available options in the software. This approach was partially successful, but the datasheet did not state the registers from which to read the measurement data, so path reached a dead end.
To overcome the lack of information, a *Saleae Logic Analyzer* was used. This analyzer, together with its *Logic 2* software, can track and record I2C bus activity, showing the voltage levels and the unencrypted data sent on the bus. The *AS7341 Demo ALS* software uses an USB dongle to convert the software inputs into corresponding I2C messages for the sensor. By connecting the analyzer to the bus lines, a complete measurement cycle - from sensor activation, through measurement, to deactivation - was recorded. The captured messaged were then analysed and compared with the apps setup and the datasheet, which not only confirmed the previously developed setup but also revealed the measurement data registers. The structure of the code is visible in figure 3.11.
The ISP2053 development board was used to test the code on the ISP2053. Therefore, the I2C pins were connected to the corresponding pins on the AS7341 development board. This allowed the entire setup to be tested without needing the custom PCBs. Both boards were powered separately with $3.7\,\mathrm{V}$ for the ISP2053 and $1.8\,\mathrm{V}$ for the AS7341.
Listing 3.1 shows how each message in the I2C protocol is constructed in the firmware. First, The target register and data are stored in the array *config*. This array is then passed to the *i2c_write_dt* function, along with the target device address. If the MCU fails to communicate with the target device, *ret* will be set to a non-zero value and an error message will be printed. In this example the sensor is enabled by setting the AS7341_ENABLE register to 1.

```
config[0] = AS7341_ENABLE;
config[1] = 0x01;
ret = i2c_write_dt(&dev_i2c, config, sizeof(config));
if(ret != 0){
    printk("Failed to write to I2C device address %x at Reg. %x \n
       ", dev_i2c.addr, config[0]);
    return -1;
}
```

Listing 3.1: I2C message implementation in C

3.2.3. Connect powered radio to personal device

This section provides a step-by-step manual of how to connect your personal phone (android or IOS) or computer to the IMT.

Android phone

1. Download the *nRF Connect* app on your phone.
2. Open the app.
3. Scan for Bluetooth devices (SCANNER tab).
4. Connect to *IMT Implant*.
5. Tab on *Battery Service*, then on the three down facing arrows to get a battery SOC approximation.
6. Tab on *Unknown Service*, then on the three down facing arrows to start the measurement.
    - *Value* gives the measured value in HEX.
7. Change LED current:
    a) 2nd *Unknown Characteristic* (**UUID: e9ea0003**).
    b) Tap on arrow.
    c) Select *UINT 16 (Little Endian)* as datatype.
    d) Choose number between 4 and 258 (mA).
    e) Click *SEND*.
8. Change LED blinking interval:
    a) 3rd *Unknown Characteristic* (**UUID: e9ea0004**).
    b) Tap on arrow.
    c) Select *UINT 16 (Little Endian)* as datatype.
    d) Choose any number between 1 and 65535 (s) (wait time between the LED turned on intervals).
    e) Click *SEND*.
9. Change sensor integration time:
    a) 4th *Unknown Characteristic* (**UUID: e9ea0005**).
    b) Tap on arrow.
    c) Select *UINT 16 (Little Endian)* as datatype.
    d) Choose any number between 0 and 65535. (Every tick increases the integration time by $166\,\mathrm{ms}$ from a $333\,\mathrm{ms}$ baseline.)
    e) Click *SEND*.
10. Swipe from left to right to see the data log in the app.
11. Copy the log or save it as a .txt file on your phone.

iPhone

1. Download the *nRF Connect* app on your phone.
2. Open the app.
3. Scan for Bluetooth devices (SCANNER tab).
4. Connect to *IMT Implant*.
5. Tab on *Battery Service* from Attribute Table to get a Battery SOC approximation.
6. Tab on *Unknown Characteristic; Properties: Read and Notify* (**UUID: e9ea0002**) starts measurement.
7. Change LED current:
   a) 2nd *Unknown Characteristic* (**UUID: e9ea0003**).
   b) Tap on arrow.
   c) Select *UINT 16 (Little Endian)* as datatype.
   d) Choose number between 4 and 258 (mA).
   e) Click *SEND*.
8. Change LED blinking interval:
   a) 3rd *Unknown Characteristic* (**UUID: e9ea0004**).
   b) Tap on arrow.
   c) Select *UINT 16 (Little Endian)* as datatype.
   d) Choose any number between 1 and 65535 (s) (wait time between the LED turned on intervals).
   e) Click *SEND*.
9. Change Sensor integration time:
   a) 4th *Unknown Characteristic* (**UUID: e9ea0005**).
   b) Tap on arrow.
   c) Select *UINT 16 (Little Endian)* as datatype.
   d) Choose any number between 0 and 65535. (Every tick increases the integration time by $166\,\mathrm{ms}$ from a $333\,\mathrm{ms}$ baseline.)
   e) Click *SEND*.
10. Swipe from left to right to see the data log in the app.
11. Copy the log or save it as a .txt file on your phone.

Windows computer

Apparently, there are some issues running a python script on macOS. To ensure proper functionality use a windows computer.

1. Open “BLEmessagesToCSV.py” in Visual Studio Code.
2. Adjust the BLE_DEVICE_ADDRESS to the one of the respective PCB.
    - The address is different for all the radio chips.
    - You can look it up, using your phone and the nRF Connect app, or just run the code on the computer and it prints all BLE devices it finds in the terminal. Scroll through the list until you find the *IMT Implant* and copy its address.
    - Looks something like this: CF:BD:E1:D7:9E:3B
3. Adjust the csv_file_path (Line 37) to a directory on your computer and name the CSV file as you like.
    - The file is automatically generated. It is not necessary to manually create it before running the script.
    - If there is already a file with the given name, the new data will be appended at the end of the existing file.
4. Make sure no phone is connected to the radio chip anymore.
5. Run the code (Radio only connects to computer if it is not connected to anything else).
6. All measurement values will be saved in a CSV file with their timestamp.

3.2.4. Improvements

Adjusting the firmware setup on the radio PCB improves the module’s current consumption significantly. Figure 3.12 shows the results at different stages of the firmware development process. Initially, the solid line in the figure represents the current consumption, averaging at $2.35\,\mathrm{mA}$, with no special power saving configurations applied at this point. In the next iteration, the power management configuration option of the nRF toolbox was utilized. Activating device power management enables device drivers which take advantage of the device power management subsystem [39]. This adjustment reduced the current consumption to the dashed line in figure 3.12, averaging $1.90\,\mathrm{mA}$. Although this was a significant reduction, it was not big enough to consider the improvements complete.
The ISP2053 module supplies the AS7341 sensor with $1.8\,\mathrm{V}$ while being powered by the battery at a nominal $3.7\,\mathrm{V}$. Further configuration changes, such as setting CONFIG_SERIAL=n and CONFIG_BOARD_ENABLE_DCDC_HV=n, reduced the current consumption to the dash dotted line in figure 3.12, averaging $0.508\,\mathrm{mA}$. The serial

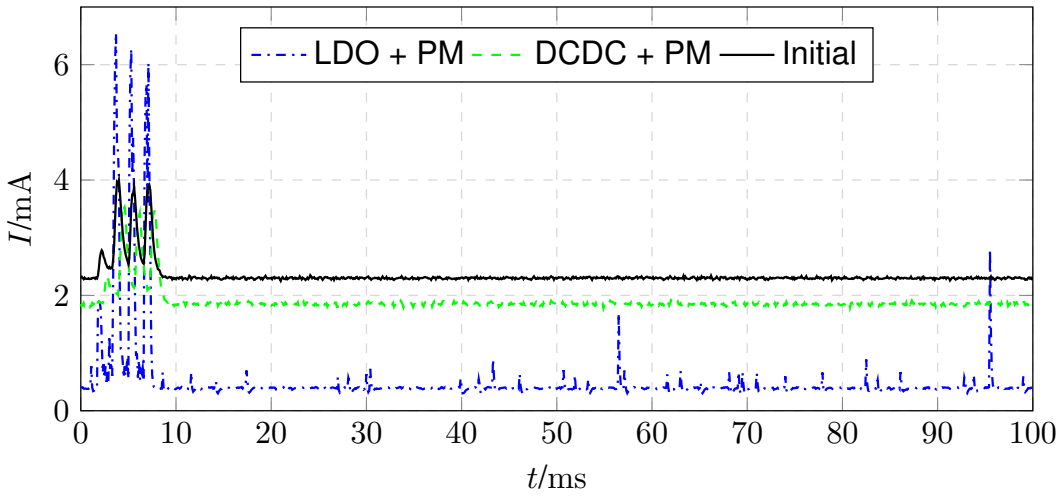

Figure 3.12.: Progress in current consumption of the IMT, by changing the power management (PM) and peripheral power setup.

configuration disables options for serial drivers, which are not necessary for the IMT system. The second change is switching from a high voltage DCDC converter to a Low Drop Out (LDO). The LDO turned out to be much more efficient than the DCDC converter for low current levels, making it the better configuration for the IMT.
Further improvements were not considered mission critical, as the current consumption achieved was sufficient for acceptable battery life in the prototype.

3.3. Optics

The entire optical system is visible in figure 3.13. This section will cover the lenses, filters and the spacer, as excitation LED and emission sensor are already discussed in chapter 3.1.

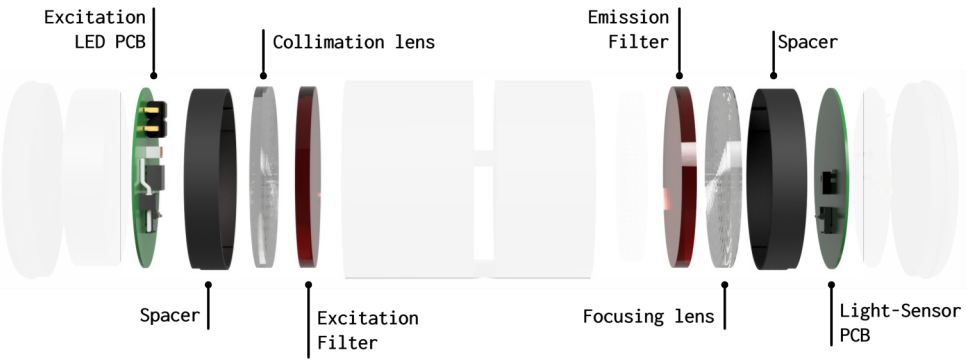

Figure 3.13.: Optical system inside the IMT.

3.3.1. Lens selection

Optical lenses serve two essential purposes in the IMT:

- They collimate or focus of light, enhancing incident power.
- They reduce of the angle of incidence on the filters, ensuring their optimal performance.

Due to the tight spatial constraints, conventional spherical lenses are not suitable. Instead, Fresnel-lenses are used. These lenses replace the curved surface with a series of concentric grooves on a nearly flat surface. The design minimizes light absorption while it passes through the lens. The grooves act as individual refracting surfaces, resembling miniature prisms in cross section, bending parallel rays with a nearly uniform focal length. However, this results in some image is distorted [40]. The Fresnel lenses are also lighter, compared to regular lenses with high volume. As both weight and space should be kept low, and the focus of the image is far less important than the low absorbance and space, Fresnel lenses are the perfect fit. The two main optics distributors for the laboratory, *Edmund Optics* and *ThorLabs*, both offer Fresnel such lenses in $25\,\mathrm{mm}$ diameter. However, the selection is limited. The *ThorLabs* lens has a $25\,\mathrm{mm}$ focal length, while the *Edmund Optics* lens only has $5\,\mathrm{mm}$ focal length [40] [41].

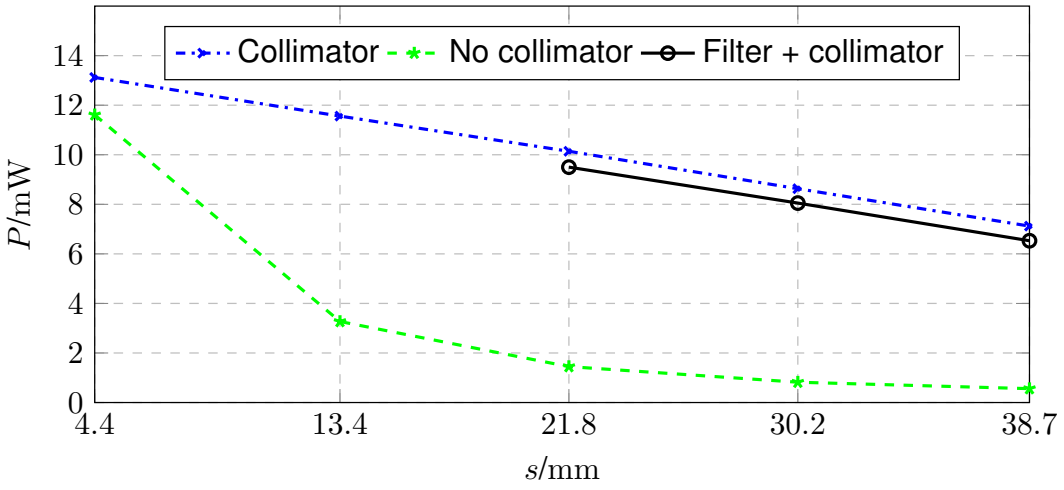

Figure 3.14.: Incident power with and without collimating optics.

Initial tests of the *Edmund Optics* lens are shown in figure 3.14. The power is measured with the *ThorLabs* PM400 power meter in all three cases: No lens, just the lens and the lens with an excitation filter. The distance on the abscissa represents the distance between the LED PCB's surface and the power meter, if no lens is used and the lens and the power meter, if a lens is used. Distance is increased by adding sample tubes to the setup.
The dash-dotted line in the graph represents the power measurement with a lens. The dashed line shows the power with neither lens nor filter. The solid line shows the incident power, using the lens and excitation filter. The minimum distance for the filter and lens

combination is bigger because two additional spacers were required to accommodate the filter. As expected, adding the excitation filter slightly decreases the power compared to the measurement with only the lens (dash-dotted line), as the filter blocks part of the emitted spectrum, leading to reduced power on the meter.
Without using a lens, the incident power decreases quickly within the first $13\,\mathrm{mm}$, dropping over $71\,\%$. In the IMT prototype, the distance will be approximately $14\,\mathrm{mm}$, so using lenses significantly increases the incident power. However, the lenses collimation is not perfect; incident power decreases by approximately $12\,\%$ with every added spacer.

To properly fit the lens into the tube system and later into the implant, it needs to be modified physically. The lens's actual part with the concentric grooves is circular, but it is delivered in a square shape. The corners need to be cut away, leaving only the concentric grooves.

3.3.2. Filter selection

The excitation light uses is relatively intense compared to the emission light for two reasons:

- Not all the excitation light hits fluorophores to be converted into the emission wavelengths.
- Fluorophores emit light in all directions randomly.

To measure low concentrations effectively, a high amount of excitation light is necessary. However, to take full advantage of this high excitation intensity,it is crucial to minimize the stray light hitting the sensor at the excitation wavelength.
As elaborated in chapter 3.1.1, a LED and excitation filter are selected to be the light source for the IMT. To enhance the signal-to-noise ratio, an additional emission filter is also required. Thus, two bandpass filters are used to protect the sensor from detecting excitation light. The first filter removes some of the excitation spectrum, allowing only a narrow band to reach the fluorophores. The second filter then blocks any remaining excitation light that has not been absorbed by fluorophores, permitting only the shifted wavelengths to pass through. Consequently, the sensor measures only the intensity of the shifted wavelength.
The filter pair must be suitable for the excitation light and the selected fluorophore. The fluorophore determines the wavelength shift and therefore the emission spectrum. For Cy5, the chosen filter combination is *Semrock* 628/40 (excitation) and *Semrock* 692/40 (emission). These filters are specifically designed for Cy5, ensuring high brightness and a good signal-to-noise ratio [42].

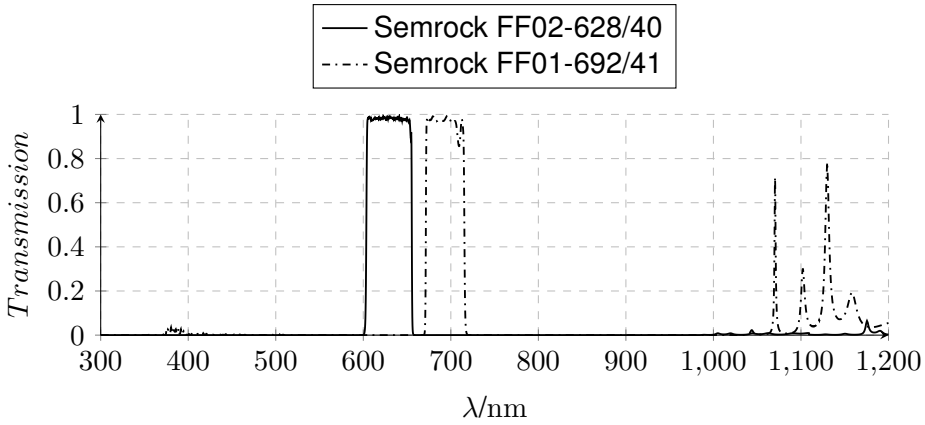

Figure 3.16.: Optical filter transmission [42].

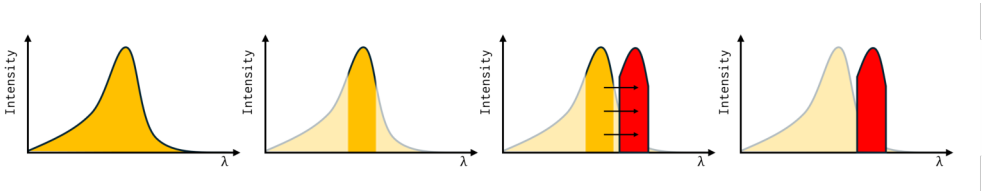

Figure 3.15.: Schematic of the spectrum propagation through the IMT. From left to right: LED excitation spectrum; Excitation filter effects; Wavelength shift by fluorophores; filtered emission light.

Figure 3.15 shows the schematic spectrum propagation through the IMT, from left to right. Initially, the LED emits a broad spectrum. This spectrum is partially blocked by the excitation filter (shown in the second picture). The fluorophores then shift the spectrum to bigger wavelengths (illustrated in the third picture). Finally, the emission filter removes the remaining excitation light, leaving only the emission spectrum. The specific transmission range for the filter pair is shown in figure 3.16.

3.3.3. Spacer

Spacers between the PCBs and lenses are necessary because of the lenses' focal length. The selected lens has a focal length of $5\,\mathrm{mm}$. To ensure the right amount of space between the lens and the PCB, a spacer is necessary.
The focal length reference point of the Fresnel lens is in the middle of the lenses' thickness.The highest light intensity was measured for a spacer height of $4.6\,\mathrm{mm}$. This measurement was done using the *ThorLabs* PM400 optical power meter and *ThorLabs* flexible tube system. The distance between PCB surface and lens was changed between $4\,\mathrm{mm}$ and $6\,\mathrm{mm}$ to find the maximum optical power.
The spacer for the IMT was then designed using *Autodesk Fusion*. It is a ring with a small cutout on one side, as visible in figure 3.17a. The cutout enables the cable that connects the LED PCB to the sensor PCB to be wired without tilting any PCB. Additionally, it is designed to block as little light as possible, while ensuring stability.

Therefore, four small sections have an increased thickness of $0.75\,\mathrm{mm}$, while the rest is $0.5\,\mathrm{mm}$ thick, see figure 3.17b.

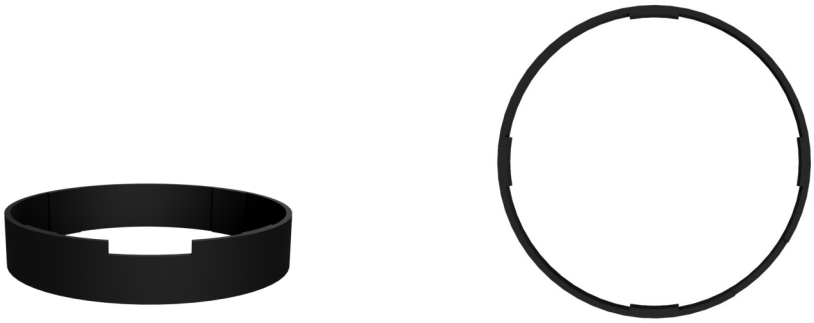

(a) Lens spacer cut out. (b) Lens spacer top view.

Figure 3.17.: Rendering of lens spacer.

3.4. Enclosure

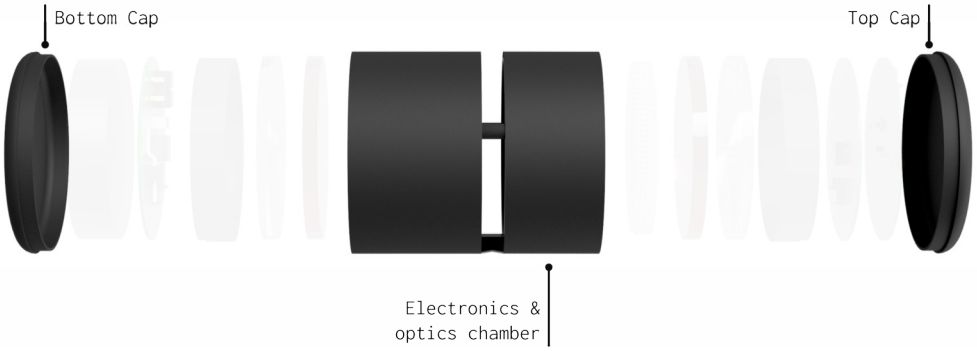

Figure 3.18.: Overview of the enclosure of the IMT.

Figure 3.18 shows the final enclosure design of the IMT highlighted in the assembly. It consists of three 3D printed parts, two slides and sealed with glue. This section will detail the design process and relevant decisions made.

The primary function of the enclosure is to protect the electronics and optics from the ISF. However, several other requirements must also be fulfilled:

- Ensure structural integrity.
- Provide two compartments for housing electronics and optics.
- Allow the sample to fit between the symmetrically arranged optics.
- Enable the electronics to be connected by wire.

3.4.1. Materials and manufacturing

All parts are printed using a *Carbon M2* 3D printer and UMA90 resin. UMA90 is a biocompatible easy-to-use resin [43].
The glue used is *Loctite* 4902. It is biocompatible and fast curing, while providing sufficient strength [44].

3.4.2. Design and components

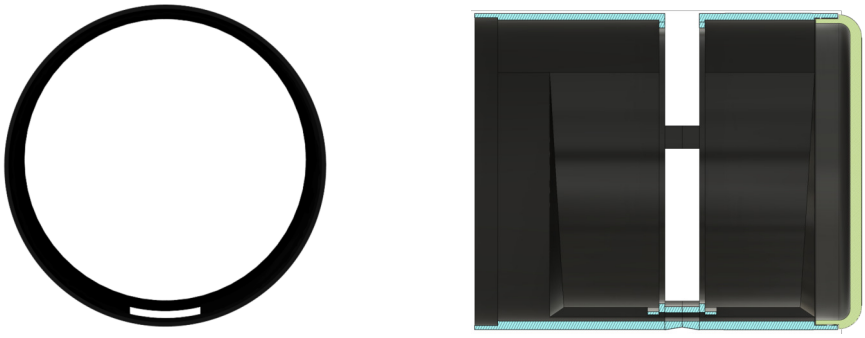

(a) Enclosure top view. (b) Enclosure cut side view.

Figure 3.19.: Rendering of enclosure.

The sensor and LED need to be in separate compartments, because the sample must be positioned between them. They must be electrically connected, as the sensor drives the LED's current. This setup is made possible with 3D printing technology.
First tests were conducted, comparing different wall thicknesses for ring-shaped designs. $1\,\mathrm{mm}$, $0.5\,\mathrm{mm}$ and $0.25\,\mathrm{mm}$ were tested. This easy design was stable for all three wall thicknesses. However, adding ledges and altering the wall thickness within the design led to printing errors for thicknesses below $0.5\,\mathrm{mm}$.
The overall design concept remained consistent throughout the process, while numerous iterations were made to improve the details and allow easy evaluation of their effectiveness. The final design is depicted in figure 3.19, showing both the cable tunnel and the support structure inside the enclosure.
The enclosure is designed to be symmetrical, housing all optics and electronics. A slit along the symmetry axis accommodates the sample scaffold, allowing the ISF to diffuse into the scaffold. The optics and electronics compartments are positioned on either side of the slit, aligned with the optical path. A small tunnel connects the compartments, providing sufficient space for a thin cable. This cable channel extends to inside the compartments, allowing the cable to rest without mechanical stress from clamping. After printing, the inner part of each compartment is sealed with a transparent slide, which is glued in place and supported by a small ledge in the print, as seen in figure 3.19b. The compartments inner diameter is $25.35\,\mathrm{mm}$, fitting the $25\,\mathrm{mm}$ optics and electronics, while leaving enough tolerance for easy assembly.
The two caps for the enclosure are identical and designed to slide into place easily,

providing a smooth closure for the implant, as shown in figure 3.19b. There is an overlap of $1.5\,\mathrm{mm}$ between the cap and the main enclosure, with the cap fitting inside the main enclosure.
A custom thread system was tested to secure the caps, offering the advantage of reusability over glue. However, this approach had drawbacks:

- poor Print print quality and
- Increased device diameter by $1.5\,\mathrm{mm}$.

Adjusting thread parameters, such as depth, width, camber and incline, did not sufficiently improve print quality, making threads an unviable option. Therefore, using glue means that the IMT must be cut open each time the battery needs recharging. This increases the assembly effort and shifts the focus towards design optimization for easy assembly.

3.4.3. Assembly process

1. Remove support structure from 3D-print (make it really smooth).
2. Drop a $25\,\mathrm{mm}$ cover glass in both electronics compartments and fix them with Loctite 4902.
    a) Push the glass down carefully on the edges. Easiest, if the side with the tunnel is down first, to avoid the ledge there.
    b) Prepare the glue (Loctite 4902, instant adhesive).
        i. Cut away the upper part of a pipette tip, about an inch. Sample cutaway is in the lower right corner of the pipette tip storage container.
        ii. Put the lower part of the pipette tip on the nozzle of the glue container. It must fit tight, otherwise it will come off while applying glue.
    c) Push out the glue in the corner between glass and 3D print. Be careful not to spill. All spillage will interfere with the signal.
    d) Make sure everything is sealed. If needed, put in several turns.
    e) Wait as long as possible for the clue to get hard (at least 10 minutes). As the glue is relatively thick in the corner, and it needs to be fully cured for the next step.
3. Fill the smaller compartment first. Make sure all the components are pushed down as far as possible.
    a) Put in the emission filter, arrow pointing towards you “^”.
    b) Put in the focusing lens, flat part towards you. Grooves towards the filter.
    c) Put in the spacer, cutout facing towards you and aligning with the tunnel.

i. Cutout needs to be on the PCB side.

ii. There is a big ($9\,\mathrm{mm}$ height) and a small ($4.6\,\mathrm{mm}$ height) spacer. The big one is only for sample pieces without optics. Use the small one for an usual implant.

d) Make sure the most recent firmware is flashed on the radio PCB.

e) Put connected sensor and radio PCBs and cable in the enclosure. Make sure the cable is going through the tunnel.

i. Connect sensor and radio PCB, using the low profile connector.

ii. Connect the 4 pin FFC/FPC cable with the sensor PCB, silver contacts visible if you look on the PCB.

f) Put cap on. **No glue yet!**

4. Fill the bigger compartment. Make sure all the components are pushed down as far as possible.

a) Put in the excitation filter, arrow pointing away from you, meaning arrow pointing the ground “v”.

b) Put in the collimation lens, flat part towards you. Grooves towards the filter.

c) Put in the spacer, cutout facing the PCB and aligned with the tunnel.

d) Connect the LED PCB with the FPC/FCC cable, silver contacts visible if you look on the PCB.

e) Snap the battery in, positive pole visible.

f) Push the PCB, with battery on top in the compartment.

5. Put cap on. **No glue yet!**

6. Functionality check:

a) Connect your phone.

b) Start a measurement.

c) If the implant starts blinking, check completed.

7. Seal both caps with the Loctite 4902 glue.

3.4.4. Testing and validation

The enclosure design was subject to regular changes. Since 3D print is relatively cheap and fast, each change was followed by a new print to asses whether the modification improved the design. Testing continues iteratively until the design met the desired standards for quality and ease of assembly. Only after achieving these standards were the tests described in this section performed.

Visual inspection

The 3D printed parts need to be thoroughly inspected for manufacturing errors, especially the main enclosure, which is prone to errors due to its complexity. The tunnel must be clear and all edges should be sharp and free of printing irregularities. Occasionally, support structure can become attached to the inside of the enclosure during the curing process. These unwanted features must be carefully removed with tweezers before assembly.
The two electronics compartments must be properly sealed to prevent any leaks that could contaminate the optics or damage the electronics. Immediately after applying glue to the slides in the implant, a visual inspection should be conducted. Moving the implant under light will help identify any reflective spots where the fresh glue is present. A thin, continuous layer of glue should be visible along the entire edge. If the glue is not spread evenly, an additional layer may be applied. Errors at this end of the assembly are difficult to detect later, making it crucial to work carefully to minimize risk of flaws.
The glue layer should also not be too thick, as this can prevent the optics from fitting properly and increase the noise level of the implant. It is important to use the pipette tip to distribute the glue evenly in a thin layer. After mounting the top and bottom caps and applying glue, another visual inspection should be performed to ensure there are no gaps in the glue film, which could compromise the enclosure's watertightness.

Leakage test

This test can not be performed with all implants, as doing so would drain the battery with the standby current. Instead, it was performed once on an implant identical in construction to the others. A fully assembled and sealed implant was submerged underwater for $24\,\mathrm{h}$. Afterward, the implant was dried externally and then opened to assess possible leakages and inspect the structure. No leakages were observed. The 3D print did soften slightly but remained intact without a significant loss of rigidity.
Take away: If properly sealed, the enclosure is watertight for extended periods of time and without losing structural integrity.

Mechanical stress test

The 3D printed enclosure is not completely rigid. It flexes under pressure without causing permanent deformation or damage. However, with all the additional components inside, there is a risk of damaging the optics or electronics. To test rigidity for the fully assembled implant, both axial and radial pressure were applied firmly by hand. All components fit tightly, which prevents any radial deformation of the implant by hand.
Axial pressure is more critical because the sample slit in the middle of the implant provides little stability. This is where the flexibility of the UMA90 material comes to play. When axial pressure is applied, the support structure bends, but does not beak.

4. Results

This chapter presents the most relevant results achieved. The system's functionality and limitations are shown.

4.1. Emission power

The emission power was tested using a 3D printed scaffold with Cy5 bound to it. This sample was inserted into the *ThorLabs* tube system equipped with the selected filters, lenses and LED. The emission power on the emission side was then measured using the *ThorLabs* PM400 power meter. The goal of this measurement was to estimate the magnitude of the emission signal under near-real conditions. Figure 4.1 shows the almost linear correlation between LED current and emission power. Based on this measurement, three current values were chosen to be used for the following measurements: $20\,\mathrm{mA}$,$37\,\mathrm{mA}$ and $50\,\mathrm{mA}$, corresponding to $5.2\,\mu\mathrm{W}$, $10.3\,\mu\mathrm{W}$ and $15.04\,\mu\mathrm{W}$ of emission power, respectively. For some measurements, more current values above and below this range were selected to broaden the scope of the results.
The emission power directly correlates with the measured ADC value, but the LED current is not the only influencing factor. The sensor's integration time also plays a significant role. For all three currents shown in figure 4.2, there is a proportional increase of ADC value with linger integration times. Doubling the integration time results in a doubled measured value, which can be used to reduce the maximum current consumption and minimize voltage drop due to high current consumption, while maintaining a strong signal. Figure 4.2 also shows the standard deviation of the measured ADC value for each current and integration time, which is too small to be clearly visible at this scale. This is desirable, as it shows that the measurements are highly consistent.

4.2. Battery life

Figure 4.3 shows the battery life of the IMT for four different LED currents. The LED was turned on with the specified current for $1\,\mathrm{s}$ in $5\,\mathrm{s}$ intervals. During the remaining $4\,\mathrm{s}$ of each interval, battery supplied only the standby current of about $0.5\,\mathrm{mA}$. As a result, doubling the LED current does not exactly halve the battery life. Especially for low LED currents the standby current is a relevant factor for battery life due to the overall lower average current draw. In the intended use case of the IMT, the time between

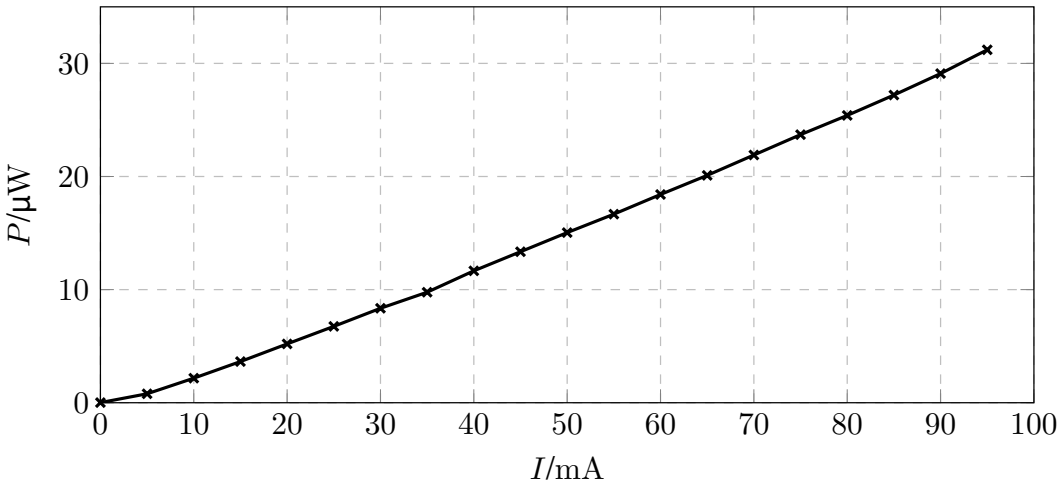

Figure 4.1.: Emission Power with Cy5 bound scaffold for different currents.

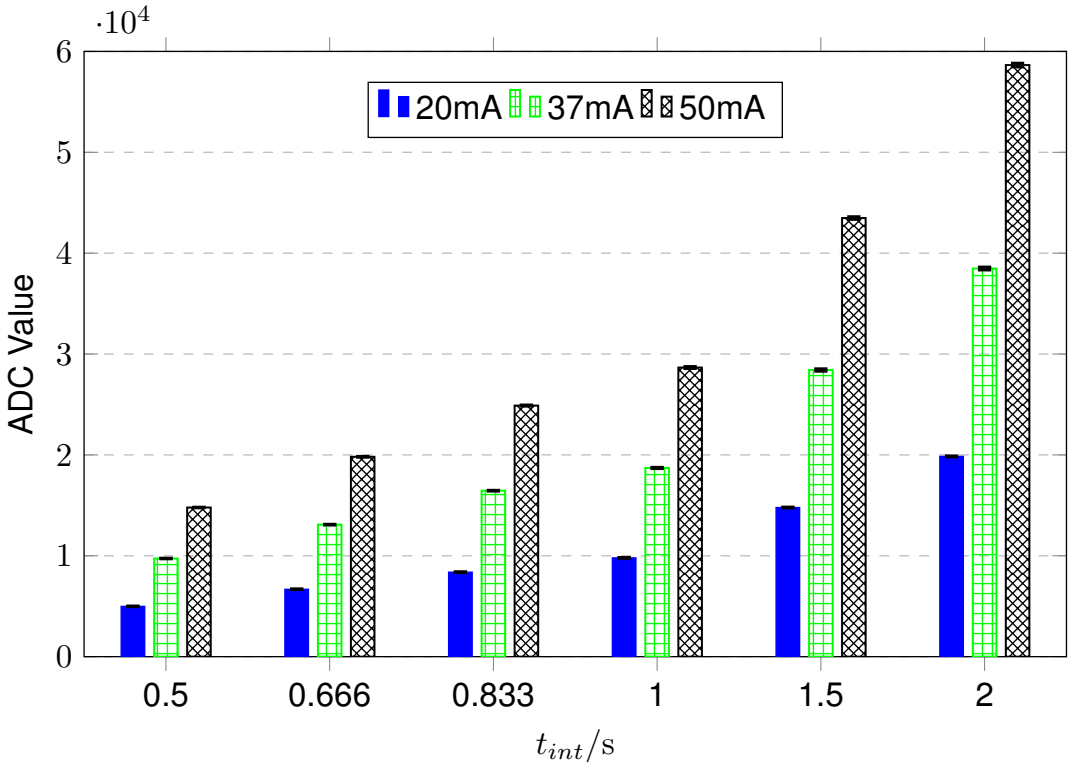

Figure 4.2.: Integration time and current variation influence the measured value

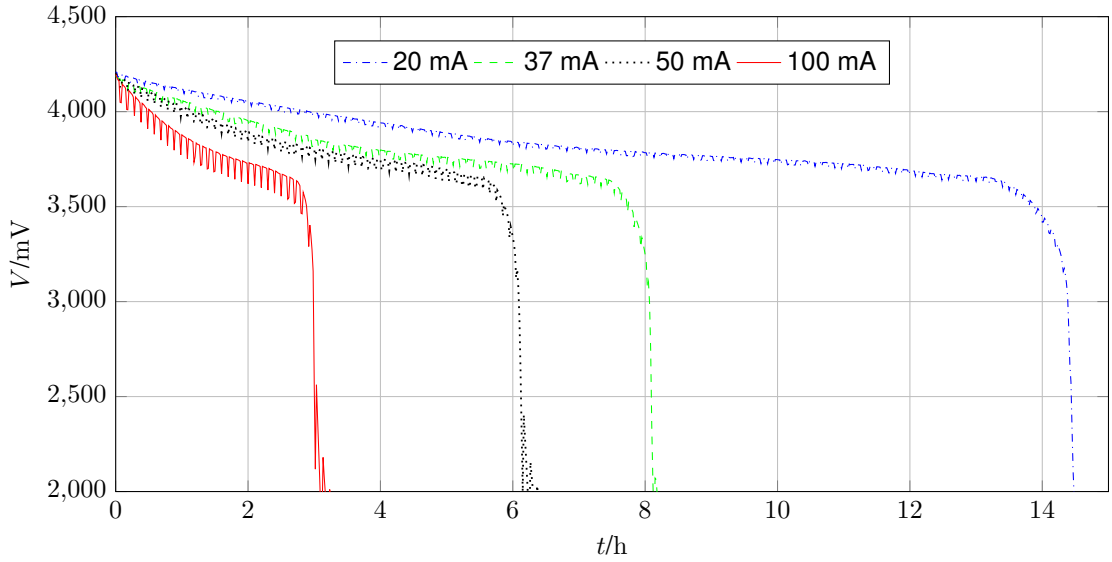

Figure 4.3.: IMT battery life for different LED currents with $5\,\mathrm{s}$ intervals and $1\,\mathrm{s}$ LED turn on time

measurements will be much longer than $5\,\mathrm{s}$, making the standby current even more important. However, this also means that the battery life will improve, as the average current draw will be lower. The initial target of an $8\,\mathrm{h}$ battery life is achieved with LED currents below $37\,\mathrm{mA}$ for $5\,\mathrm{s}$ intervals.
Regardless of the LED current, the battery will eventually be fully drained, causing the cell voltage of the lithium ion battery to drop below $2\,\mathrm{V}$. When this happens, the electrical system enters a parasitic battery saving state. The LED itself requires about $1.7\,\mathrm{V}$ of forward voltage to draw significant current, plus some headroom is required for the LED driver to setup the current properly. If the LED is turned on, the battery voltage drops further due to the increased load. The combination of these factors prevents the LED from turning on after the battery voltage drops below $2\,\mathrm{V}$, reducing power consumption and preventing deep discharge.

4.3. Voltage drop

Figure 4.4 shows the battery voltage drop due to the current drawn by the LED for the four different currents also used for the battery life measurement. It captures a $6\,\mathrm{s}$ snapshot from the battery life plot (figure 4.3), shortly after the test started. The slightly different initial voltages in the beginning - $4.2\,\mathrm{V}$ for $20\,\mathrm{mA}$ and $50\,\mathrm{mA}$, $4.18\,\mathrm{V}$ for $37\,\mathrm{mA}$ and $100\,\mathrm{mA}$ - are likely the result of charging the battery at either $40\,\mathrm{mA}$ or $20\,\mathrm{mA}$ in the charging station. This small difference was not identified until after all measurements were done.
Nevertheless, it is clearly visible in figure 4.4 that the voltage drop correlates with the LED current. The dash dotted line for $20\,\mathrm{mA}$ has the smallest, the solid line for $100\,\mathrm{mA}$ the largest voltage drop. The voltage remains stable when the LED is off. The moment the LED draws current and turns on, the voltage drops by up to $0.1\,\mathrm{V}$. After the LED is

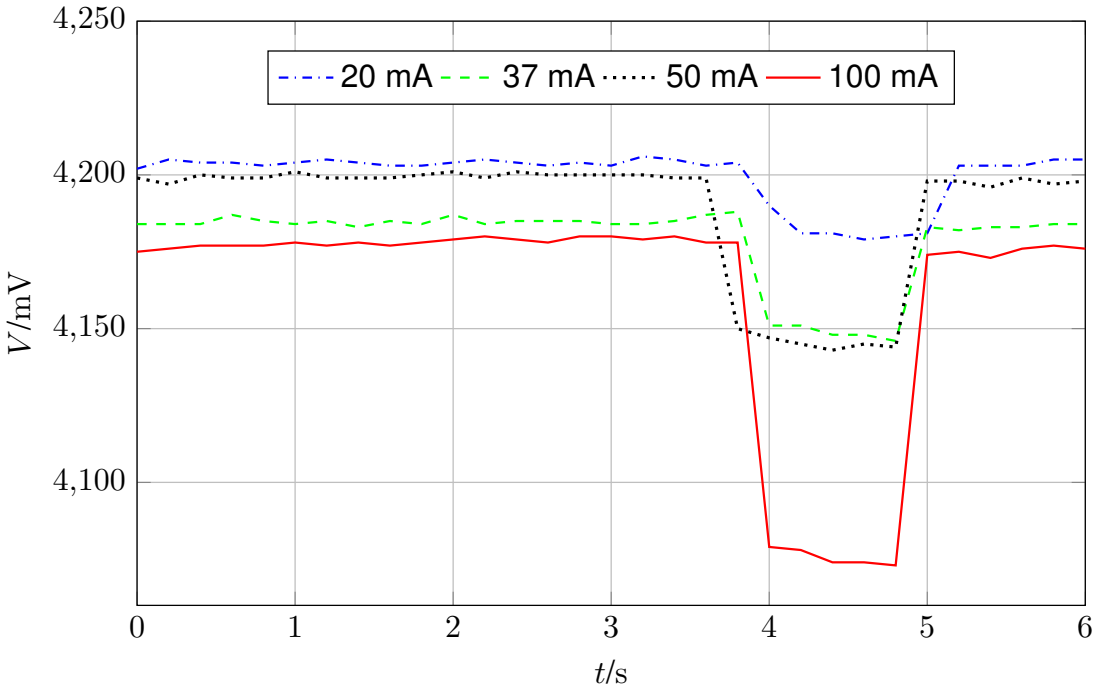

Figure 4.4.: Battery voltage drop due to LED current

turned off again, the voltage recovers to almost the same level as before. These voltage changes are also visible in the battery life plot, as indicated by the ripples in figure 4.3.

4.4. Limit of detection

To properly characterize the measurement capabilities of the IMT, the Limit of Detection (LOD) crucial. The results of this test will help the molecular side of the project estimate of how many sensing switches are necessary to detect a signal. While these measurements were taken in an idealized environment with minimal noise, they still provide a baseline of what is achievable.

For the LOD test, pure Cy5 dye was diluted in water, starting from an initial concentration of $2\,\mathrm{mM}$. This solution was then diluted in four steps. First, $15\,\mu\mathrm{L}$ of the $2\,\mathrm{mM}$ Cy5 solution was diluted in $30\,\mathrm{mL}$ of water to achieve a concentration of $1\,\mu\mathrm{M}$. The next three steps added $30\,\mu\mathrm{L}$ of the previous solution into $30\,\mathrm{mL}$ of water, reaching a final concentration of $1\,\mathrm{fM}$. The $30\,\mathrm{mL}$ water was poured by hand, not pipetted, so the concentrations are approximate. The goal was to determine the detectable order of magnitude rather than exact values, making this approach sufficient.

A baseline measurement was first performed using water before the IMT was immersed in the Cy5 solutions, starting from the lowest concentration and working the way up to the highest, to prevent contamination. Higher concentration solution was added into the lower concentration solution to increase the concentration by one and two orders of magnitude, before putting the IMT into the next cup with higher concentration. For each concentration, different LED currents were set. To ensure consistency, all measurements

were performed twice with fresh dilutions and a new IMT.

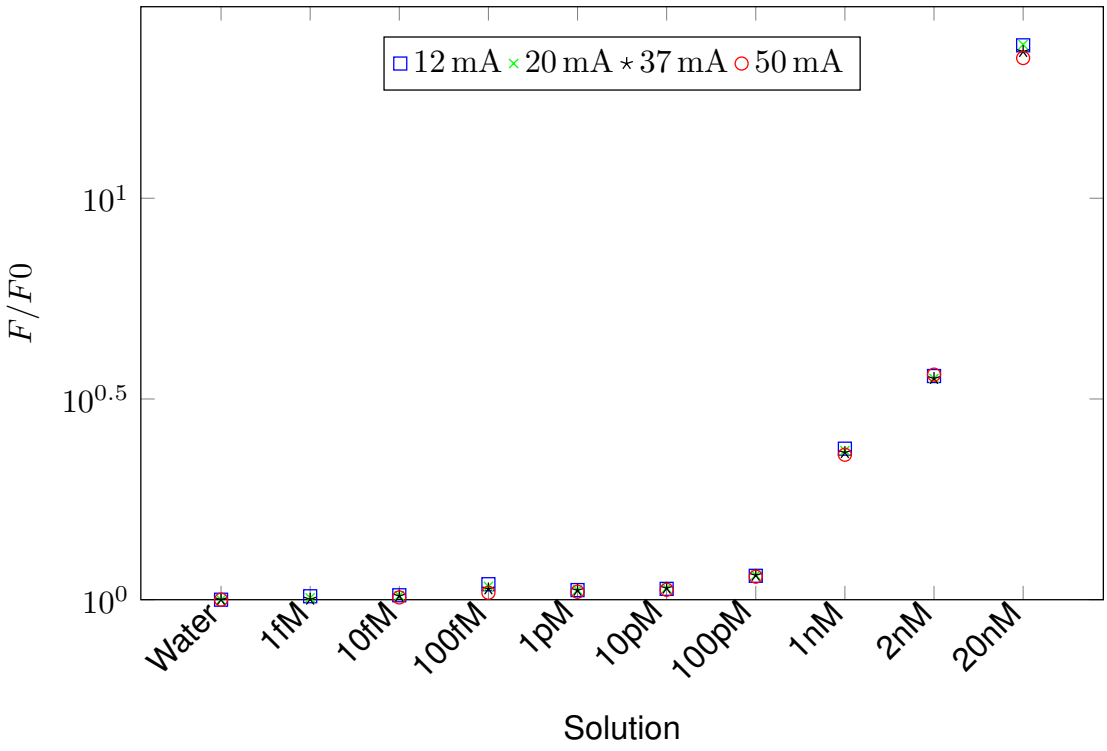

Figure 4.5.: Complete concentration range of the LOD measurement with data normalized to water and both axis in logarithmic scale (except the $1\,\mathrm{nM}$ - $2\,\mathrm{nM}$ step), using $12\,\mathrm{mA}$, $20\,\mathrm{mA}$, $37\,\mathrm{mA}$ and $50\,\mathrm{mA}$ LED current.

Figure 4.5 provides an overview of the measurement results for various LED currents: $12\,\mathrm{mA}$, $20\,\mathrm{mA}$, $37\,\mathrm{mA}$ and $50\,\mathrm{mA}$. The data is normalized to the water reference for different concentrations. The normalized measurement values remain almost constant across all four LED currents, suggesting that the LED current has little effect on the normalized values. The noise floor for the water baseline increased with higher currents, but the signal output for the Cy5 was also proportionally greater at higher currents. The plot can be divided into two parts: From $1\,\mathrm{fM}$ to $10\,\mathrm{pM}$, where there is barely any detectable signal and from $100\,\mathrm{pM}$ onwards, where reliable signal detection is possible due to high normalized measurement values.

Figure 4.6 shows how the normalized measurement values for four different Cy5 concentrations remain constant across a range of LED currents, from $4\,\mathrm{mA}$ to $150\,\mathrm{mA}$. Concentrations below $100\,\mathrm{pM}$ were neglected in this figure because they were too close to the baseline measurement with water. Although $4\,\mathrm{mA}$ shows some deviation from the trend for all other currents, it still provides an acceptable result. All the depicted concentrations can be differentiated across these currents. These results were surprising, as previous experiments with Cy5 solutions suggested that increasing the LED current would lower the LOD, resulting in a plot of increasing normalized values with higher currents, up to a certain point, where the leakage through the filters and other parasitic behaviours became to big. This discrepancy may be due to differences in experimental setups. The previous experiments used the *ThorLabs* tube system with larger distance

between the optics and the LED and sensor compared to the IMT.
It is a encouraging to see that the normalized measurement values remain stable across a wide range of LED currents. This means that a second revision of the IMT might be powered by silver oxide batteries.

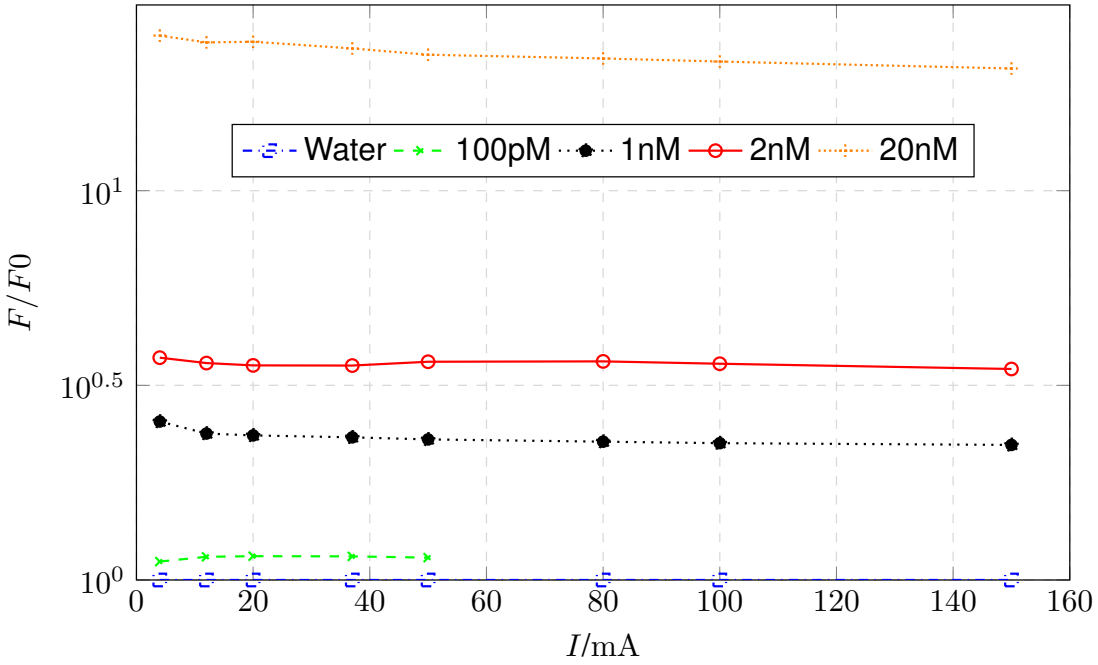

Figure 4.6.: Normalized measurement value for different solution concentrations over current range.

Although figure 4.5 indicates that concentrations below $100\,\mathrm{pM}$ are challenging to detect reliably, focusing on absolute values instead of normalized ones reveals that very low concentrations can still be detected. Figure 4.7 shows measurements done twice independently - blue and green dataset - with consistent results. Both axes use logarithmic scales, so ideally, the data should form a line with constant slope, it does not. The dashed lines in blue and green indicate plus or minus three standard deviations of the average ADC value for water, while the dotted lines indicate plus ten times the standard deviation. Each measurement point also includes an error bar of plus or minus one standard deviation. The LOD is defined as three times the standard deviation, while Limit of Quantification (LOQ) is ten times.
For $1\,\mathrm{pM}$ in dataset 2, the measurement failed, which was only realized after the experiment was finished. Therefore this measurement is deleted out of the graph.
Based on these thresholds, the LOD is $1\,\mathrm{fM}$ and the LOQ is $10\,\mathrm{fM}$, but it is important to note that this is only detectable with the water baseline calibration. The ADC value for water varied significantly between measurements (from 187 ticks to 323 ticks), but when plotted with separate y axes and aligned to the water baseline, both show similar patterns, as shown in figure 4.7. This is both positive and negative. While it is promising that a concentration of $1\,\mathrm{fM}$ can be distinguished from water, the baseline variation of $70\,\%$ between the measurements, compared to a $15\,\%$ change in the $100\,\mathrm{pM}$ Cy5 solution,

means that all measurements must be interpreted alongside a water baseline calibration.

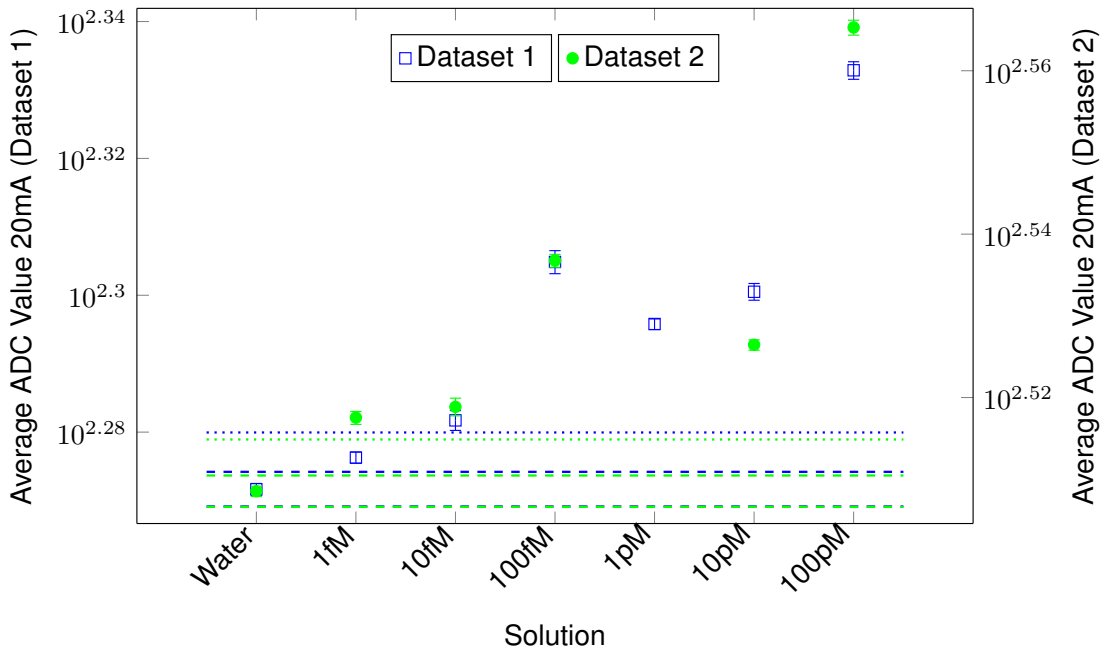

Figure 4.7.: Low concentration with error bars and indicated water baseline. Logarithmic scale for both axis. Dashed line indicates 3σ, dotted line 10σ.

The relevant value here is not the concentration, but the number of Cy5 molecules in the measurement chamber of the implant. Essentially, the LOD measurement reflects not the concentration of the biomarker but the minimum number of Cy5 molecules required for the IMT's electronics to detect a signal. With an active measurement volume of $1800\,\mathrm{mm}^3$, a $1\,\mathrm{fM}$ concentration corresponds to $1.1 \cdot 10^6$ Cy5 molecules. At such low molecule counts, signal variations due to molecule movement in the solution will be relevant, partially explaining the big difference between datasets, particularly at $1\,\mathrm{fM}$ as shown in figure 4.7. Increasing the sensor's integration time could reduce that effect, but the variations will still be bigger at lower concentrations than at higher ones.

4.5. In vitro

Initial tests of the IMT with a scaffold with aptamer switches attached were performed in vitro. For these tests, a scaffold was fixed inside the measurement chamber. Two cups, one containing Deionized (DI) water, the other a buffer solution, were prepared. Both cups were large enough to fully submerge the IMT.
DI water activates all the aptamer switches, while the buffer solution deactivates them. Figure 4.8 shows the propagation of the measurement values over time. At $t = 0$, the IMT was submerged in the DI water. At $t = 300\,\mathrm{s}$, the IMT was transferred from the DI water to the buffer solution. At $t = 600\,\mathrm{s}$, it was put back into the DI water. The measurement was done continuously with a $0.2\,\mathrm{Hz}$ frequency and $50\,\mathrm{mA}$ LED current.

The dip at $t = 600\,\mathrm{s}$ is likely due to the IMT not being fully submerged in either fluid while transitioning. Despite this, it is clearly visible how the signal changes over time as the liquids diffuse into the scaffold and react with the aptamer switches. For the buffer solution, the $5\,\mathrm{min}$ interval appears sufficient to deactivate almost all aptamers. However, for the DI water, the results are less clear. It seems the IMT should have remained in the DI water for a longer period, as the signal continues to increase at nearly the same rate all the time. When the IMT was placed in DI water for the second time, the signal increased at a lower rate than the first time. This might be due to residual buffer still present in the scaffold, requiring time for the water to counteract the buffer's effects.
The difference between highest and lowest measurement value is in the range of 1000 ADC ticks, which is approximately $1.5\,\%$ of the available dynamic range. Considering that this is the maximum possible signal amplitude, this is not too promising.

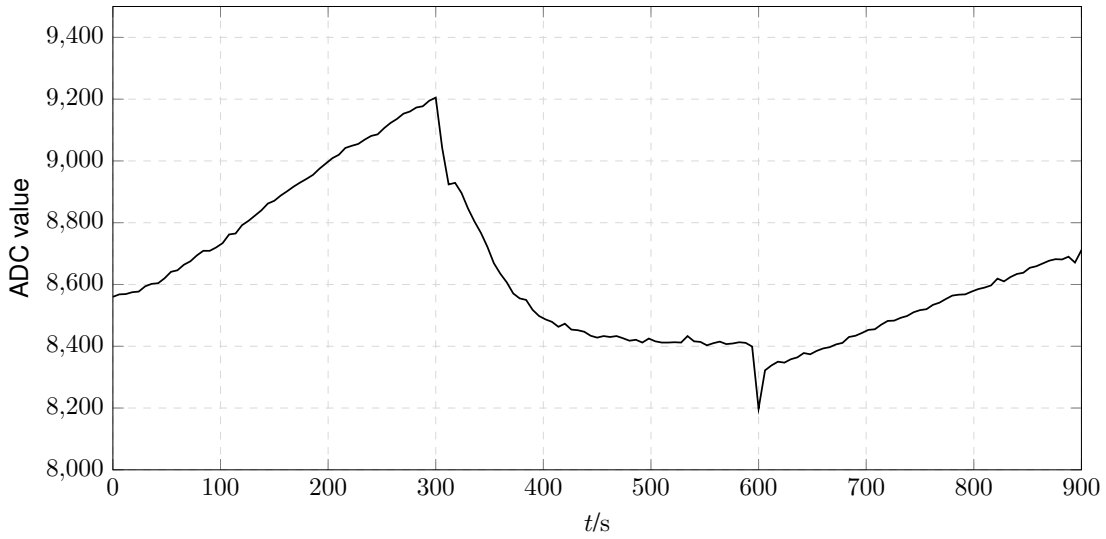

Figure 4.8.: In vitro measurement signal over time with aptamer switches, changing from deionized water to 1x buffer and back to deionized water in $5\,\mathrm{min}$ intervals.

4.6. In vivo

To evaluate the performance of the IMT living organisms, animal tests were conducted using rats. Figure 4.9 shows the implantation of the IMT into a rat. The IMT is positioned on the back of the rat, between the skin and muscle tissue. In vivo measurements are necessary, because there are two main differences, compared to in vitro measurements:

- The mount of available liquid.
- The movement of the IMT.

For in vitro experiments, the IMT was placed in a container full of liquid, allowing the solution to quickly react with the aptamer switches. However, in the rat, there is only little ISF available, increasing the diffusion time for the rat's ISF into the 3D printed scaffold

with aptamers attached. The increased diffusion time is a current limitation of this setup and could be effectively by reducing the implant's diameter.

Figure 4.9.: IMT implantation into a rat.

Figure 4.10 shows the results from the first IMT implantation in a rat. The data has been normalized, using the lowest measurement value as the reference point. During the recording there were issues with the MAC environment, randomly stopping the measurement, resulting in the big gaps between some data points.
At approximately $t = 40\,\mathrm{min}$, the rat woke up from anesthesia and began moving around in its enclosure. Although the uric acid level remained constant, big changes were detected in the measurements, likely due to increased contact between the IMT and ISF. From $t = 70\,\mathrm{min}$, the rat became inactive again, resulting in stable measurement values. The signal decrease at the end could be due to photobleaching of the fluorophores, but this was not specifically investigated at this stage.

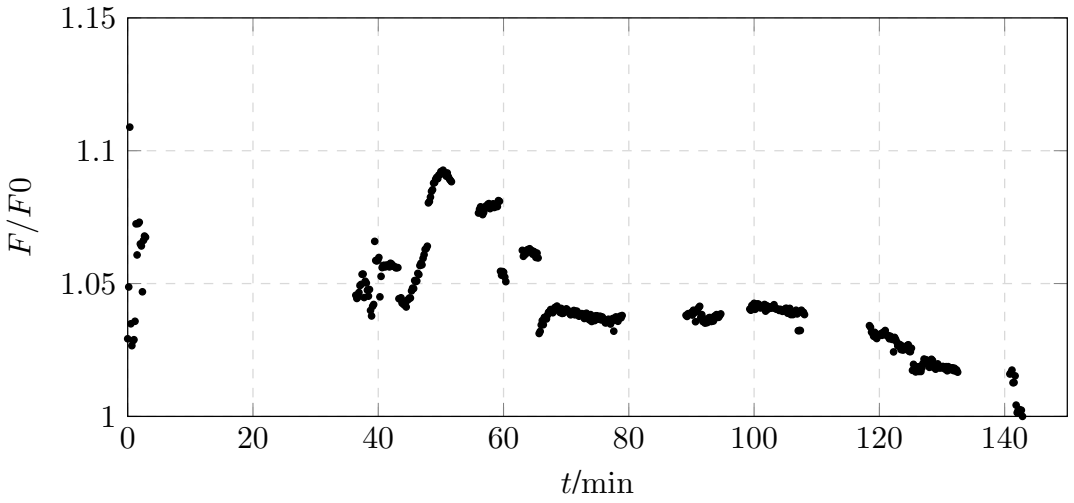

Figure 4.10.: In vivo measurement signal over time with aptamer switches, rat awake. The measurement stopped several times for unknown reasons, when run on a Mac resulting in the gaps in the plot. Values are normalized to the lowest measurements value.

4.7. Specification sheet

Table 4.1.: Summary of the IMT's specifications

Physical dimensions	
Size	$\varnothing 27.5\,\mathrm{mm} \times 36.5\,\mathrm{mm}$
Weight	$20.3\,\mathrm{g}$
Electrical	
Operating voltage	$2.8\,\mathrm{V}$ to $4.2\,\mathrm{V}$
Current consumption (LED turned off, average)	$508\,\mu\mathrm{A}$
Current consumption (LED turned on, $20\,\mathrm{mA}$)	$20.97\,\mathrm{mA}$
Current consumption (LED turned on, $37\,\mathrm{mA}$)	$38.75\,\mathrm{mA}$
Current consumption (LED turned on, $50\,\mathrm{mA}$)	$54.53\,\mathrm{mA}$
Optical	
Focal length	$5\,\mathrm{mm}$
Excitation wavelength	$605\,\mathrm{nm}$ to $650\,\mathrm{nm}$
Fluorophore	Cy5
Enclosure	
Material	Carbon UMA90
Sealant glue	Loctite 4902
Detection limit	
LOD (3σ above noise floor)	$1\,\mathrm{fM}$
LOQ (10σ above noise floor)	$10\,\mathrm{fM}$

5. Discussion

This chapter highlights the challenges and discuss the results of this project. The challenges can be divided into tow categories, hardware and molecular. As the author mainly focused on the hardware side of the project, the main focus of this discussion will also be on this part.

5.1. Hardware challenges

5.1.1. Energy storage

The lithium-ion battery was the right decision for the prototype, enabling tests with high currents while still maintaining long battery life. However, it is not possible to use this battery type in an implant for humans. To make the system compatible with other energy sources and meet legal requirements, two main challenges need to be addressed:

- Reducing peak current consumption and
- Ensuring sufficient battery capacity.

Reducing peak current consumption is mandatory to be able to use alternative energy storage options. Silver-oxide batteries are not rechargeable and can not handle big LED currents, while maintaining sufficient battery life. So, the standby current consumption must also be minimized to extend battery live. However, non-rechargeable batteries will be fully discharged at some point, rendering the implant useless.
The second option is a wireless power transmitter. Advantages of this approach are smaller implant sizes and easier battery replacement, outside the human body, making the implanted electrical system last indefinitely. On the other hand, wireless power transfer requires an external device, which adds complexity to the system and makes it impractical to use.

Although wireless power transfer was ruled out in the beginning of the project, because no external devices should be used, that might be the only viable option for the implant to achieve market success. Adding capacitors to the electrical system to buffer higher loads during the LED's on-time might be all the energy storage needed in the implant, especially if the peak LED currents can be sufficiently reduced.

5.1.2. Power management

Power management is closely related to the energy storage challenge. Postponing the start of the battery drainage to the moment the implant is used, instead of starting when it is fully sealed, is critical to use it as an off the shelf product. Right now, the battery will be discharged about six days after sealing it, even without use. This is not acceptable for a final product. At least, there needs to be an activation mechanism to start the battery life, once the implant is in use. Additionally, the average current consumption needs to be reduced further, reaching close to $2\,\mu\mathrm{A}$ during standby, which corresponds to the ISP2053's sleep current. One idea for this activation mechanism could be a reed switch with a little magnet attached that keeps the circuit open. When the user removes the magnet, the reed switch closes and completes the circuit.
Implementing a wireless power transfer to the implant would make this consideration meaningless, as it is easy to recharge or turn off the external device and thereby the implant.

5.1.3. Size

Currently, the diameter of all the electronics and optics inside the IMT is $25\,\mathrm{mm}$. This size provides sufficient space on the PCBs to add hardware debugging infrastructure and enables the use of standardized $25\,\mathrm{mm}$ diameter optics. Now, that the electrical system works, a lot of the debugging infrastructure can be removed, enabling the system to become smaller.
Cutting the diameter in half is relatively little effort. The PCBs might need four instead of two copper layers, but there will still be enough space to fit all the selected components. Reducing the diameter further would require removing the ISP2053 module, as it is square with $8\,\mathrm{mm}$ edges. The nRF5340 radio chip, inside the ISP2053, is square with $4\,\mathrm{mm}$ edges. So, the nRF5340 chip would be needed. Using that chip without the module adds peripheral circuits and antenna matching to the PCB. This makes the development far more complicated but ultimately is possible.
Moving from radial to axial size. Removing the battery saves about $5\,\mathrm{mm}$ in length, as the battery holder can be removed as well, if wireless power transmission is implemented. The power transmission needs pick up coils, though. They are most likely positioned around all other components, adding a little radial size. The optical filters used at the moment add $2\,\mathrm{mm}$ each. It might be a viable option to look for custom filters on the LED lens and just in front of the sensor, using the space between the two and their respective collimation and focusing lenses. Further improvements can be made with new lenses: As the diameter decreases, there might be lenses with smaller focal lengths available.

5.1.4. Limit of detection

Detecting $1\,\mathrm{fM}$ Cy5 diluted in water was a surprising achievement of the IMT, but this sensitivity can only be confidently achieved with a previously set benchmark in water. The individual measurements, especially when comparing several different implants, vary too much to provide meaningful results without this calibration step. These variations between devices may be due to the assembly process, such as using slightly different amounts of glue, which could cause minor changes in the angles of the filters and lenses. Nevertheless, this alone does not fully account for differences in the gain factor of the ADC values. Misalignment of the LED and sensor could also contribute, as improper alignment might prevent the chamber from being uniformly illuminated or restrain the sensor from capturing emissions from parts of the chamber.
Therefore, further LOD tests are necessary to identify the exact causes of the baseline and gain shifts.

5.1.5. In vitro

The in vitro tests were successful, but the maximal possible signal change was only $1.5\,\%$ of the available dynamic range, raising questions about the LOD when using aptamers. Increasing the time of the IMT being in the DI water might lead to larger signal differences. However, having to wait for the measurement signal to settle for extended periods presents a challenge, as it prevents rapid detection of the biomarker levels in the ISF.

5.1.6. In vivo

The in vivo tests showed some challenges with the implementation of the IMT inside the rat. There are several new unknown parameters to the overall behaviour, with movement of the rat being one of them. The skill-set for surgery was sufficient. However, the in vitro tests have to provide more positive results to characterize the implant, before doing further in vivo tests is useful.

5.2. Molecular challenges

5.2.1. Aptamer density

Essentially, the detectable signal depends on the number of aptamer switches on the 3D printed scaffold. Therefore, the aptamer density is crucial, especially if the implants diameter is reduced. The LOD measurements in chapter 4 show the minimum required number of fluorophores to detect a signal with the electrical system. This number does not take aptamer switching noise into account and is likely to be higher in real conditions.

Furthermore, the 3D printed scaffold itself absorbs and deflects some of the emission light, reducing the signal intensity further. The exact absorption and deflection values are not known at the moment.

5.2.2. Aptamer durability

Aptamer longevity is an issue with unknown parameters. It has not been tested how long the aptamer switches can survive in the body. Furthermore, measurements need to be done in constant intervals throughout the day, no matter if the patient moves or rests. Movement might change the flow of ISF into the scaffold, altering the diffusion time or signal in the process. Changing ISF composition and pH value may damage the aptamers.

5.2.3. Diffusion tpime

Opposing to the aptamer density challenge, the diffusion time improves with decreasing implant size. For the $25\,\mathrm{mm}$ diameter, it takes up to $10\,\mathrm{min}$ for fluid to fully diffuse into the scaffold. As there is only a little ISF in the body, the main contact point between ISF and scaffold is the small surface on the side of the scaffold, not the big top and bottom surfaces, making the diffusion time much longer, the bigger the diameter.

6. Conclusion

The primary objective of this thesis was to develop a functional prototype of an optical implant capable of measuring uric acid levels in ISF. To achieve this, it was essential to design and develop the necessary electronics and firmware to ensure a battery life of at least eight hours. In addition, careful selection of optical components and the creation of a suitable enclosure were critical to housing all components and protecting them from the ISF environment. The successful development of this prototype serves as proof-of-concept, demonstrating the feasibility of using aptamers with reversible binding to monitor changing levels of specific biomarkers. While uric acid was the initial focus, this technology paves the way for future projects targeting other critical biomarkers, such as cardiac troponin, which could potentially detect heart attacks before they occur.
The electrical system consumes about $500\,\mu\mathrm{A}$ in standby condition. Remote adjustment of LED current, measurement intervals, and sensor integration time is possible through the implemented BLE functionality. Testing revealed that the prototype can achieve a battery life of up to $14\,\mathrm{h}$ with a $20\,\mathrm{mA}$ LED current and a 1-second measurement interval within a 5-second cycle. Given that the blinking frequency will be lower during animal tests, the battery life is expected to increase further. The 3D printed enclosure provided sufficient structural integrity and facilitated the sealing of the implant. Sensitivity tests using Cy5 diluted in water resulted in a LOD of $1\,\mathrm{fM}$, which was confirmed in two independent iterations with a margin exceeding three times the standard deviation of the water baseline measurement. The defined threshold for the LOQ, set at ten times the standard deviation, was achieved at $10\,\mathrm{fM}$. Interestingly, the LED current had minimal impact on these results, with no significant change in LOD or LOQ detected across a range of $12\,\mathrm{mA}$ to $50\,\mathrm{mA}$.
Achieving a $1\,\mathrm{fM}$ LOD corresponds to approximately $1.1 \cdot 10^6$ Cy5 molecules in the measurement chamber of the implant. Consequently, the molecular side of the project requires at least this number of switching aptamers to produce a detectable signal. It is likely that an even greater number of aptamers will be necessary, as their presence increases the noise floor and the standard deviation of measurements. Nonetheless, this work has demonstrated that it is feasible to use switching aptamers as intended, with reversible binding.
The hardware developed in this thesis offers a versatile platform for testing various aptamers designed to bind to different biomarkers. Previous designs were confined to a stationary setup on a desk, requiring significant space and lacking the capability to be tested in real-world conditions. However, challenges remain. The standby current is not sustainable for long-term use, as it drains the battery within six days without

taking measurements. This issue must be addressed to improve the overall product. Additionally, the LOD measurements were performed under ideal conditions and must be repeated using the scaffold and aptamers once the molecular challenge of achieving high-density aptamer binding to the scaffold is resolved. Furthermore, the hardware, in its current form, is too large for practical use in humans. Both the diameter and length must be significantly reduced to make the implant more acceptable and less restrictive for patients.

The primary hardware challenge moving forward is to reduce the size of the implant while maintaining or improving battery life. This may require the implementation of wireless power transfer to the implant. On the molecular side, increasing the aptamer lifetime and packing density are critical challenges that must be defined and overcome to realize a smaller, permanently implanted device.

Further data collection with the IMT will be done in a forthcoming research paper, titled "Wireless, implantable device for real-time, continuous uric acid sensing in freely-moving animals" by Jean Won Kwak, Philipp Thoma, et al. (in preparation). Readers are encouraged to look for this publication for more data and results related to the IMT's usecase.

The IMT represents a potential breakthrough in healthcare. The ability to monitor critical biomarkers in real-time, without the need for blood samples and complex analysis, has the potential to improve the lives of countless individuals worldwide. From medically necessary applications to use by professional athletes, the IMT could become as widespread as glucose monitors are today. The hardware developed in this project not only shortens testing times for new molecular structures, but also lays the groundwork for achieving this long-term vision.

Bibliography

[1] O. Adeniyi *et al.* (2021) Monitoring biomarker. [Online]. Available: https://www.ncbi.nlm.nih.gov/books/NBK402282/

[2] N. J. Gonter. (2023) Uric acid - blood. [Online]. Available: https://medlineplus.gov/ency/article/003476.htm

[3] S. Thompson. (2021) How long does it take to get results of blood tests? [Online]. Available: https://nortonhealthcare.com/news/how-long-do-blood-test-results-take/

[4] M. Friedel *et al.*, "Opportunities and challenges in the diagnostic utility of dermal interstitial fluid," *Nat. Biomed. Eng*, no. 7, p. 1541–1555, 2023.

[5] L. Cohen and D. R. Walt, "Highly sensitive and multiplexed protein measurements," *Chemical Reviews*, vol. 119, no. 1, pp. 293–321, 2019, pMID: 30152694. [Online]. Available: https://doi.org/10.1021/acs.chemrev.8b00257

[6] Medtronic. (2019) Pillcam™ sb 3 capsule endoscopy system. [Online]. Available: https://www.medtronic.com/covidien/en-us/products/capsule-endoscopy/pillcam-sb3-system.html

[7] IntroMedic. (n.d.) Innovative capsule endoscope. [Online]. Available: https://www.medtronic.com/covidien/en-us/products/capsule-endoscopy/pillcam-sb3-system.html

[8] L. Chongqing Jinshan Science & Technology (Group) Co., "Capsule endoscopy system," https://www.jinshangroup.com/uploads/file/2024-01-24/HD_Brochure_1023.pdf, 2023.

[9] Olymups, "Smart and safe, endocapsule 10," https://mdc.olympus.eu/asset/084438885177/5d0af142e2e8473ef0654924591fe3ae, 2021.

[10] C. Inc. (2023) Capsovision product specifications. [Online]. Available: https://capsovision.com/physicians/product-specifications/

[11] L. RF Co. (2018) Sayaka the next generation capsule endoscope. [Online]. Available: https://rfsystemlab.com/en/sayaka/

[12] P. Demosthenous, C. Pitris, and J. Georgiou, "Infrared fluorescence-based cancer screening capsule for the small intestine," *IEEE Trans Biomed Circuits Syst.*, vol. 10, no. 2, pp. 467–476, 2016. [Online]. Available: https://ieeexplore.ieee.org/stamp/stamp.jsp?tp=&arnumber=7217853&tag=1

[13] M. A. Al-Rawhani, J. Beeley, and D. R. S. Cumming, "Wireless fluorescence capsule for endoscopy using single photonbased detection," *Sci Rep*, vol. 5, no. 18591, 2015. [Online]. Available: https://www.nature.com/articles/srep18591#citeas

[14] S. J. Walters, "Senseonics the next generation of continuous glucose monitoring," https://www.senseonics.com/ /media/Files/S/Senseonics-IR/documents/publications/uk-public-health-service-publication.pdf, n.d.

[15] I. A. Thompson *et al.*, "An antibody-based molecular switch for continuous small-molecule biosensing," *Science Advances*, vol. 8, no. 38, 2023. [Online]. Available: https://www.science.org/doi/10.1126/sciadv.adh4978

[16] M. Monici, "Cell and tissue autofluorescence research and diagnostic applications," ser. Biotechnology Annual Review. Elsevier, 2005, vol. 11, pp. 227–256. [Online]. Available: https://www.sciencedirect.com/science/article/pii/S1387265605110072

[17] L. L. science solutions. (n.d.) sulfo-cyanine5 nhs ester. [Online]. Available: https://www.lumiprobe.com/p/sulfo-cy5-nhs-ester

[18] ATTO-TEC. (n.d.) Atto 643. [Online]. Available: https://www.atto-tec.com/ATTO-643.html?language=en

[19] S.-Y. Yang *et al.*, "Powering implantable and ingestible electronics," *Adv Funct Mater*, vol. 31, no. 44, 2021. [Online]. Available: https://www.ncbi.nlm.nih.gov/pmc/articles/PMC8553224/

[20] M. Amaral, F. do Vale, J. Silva, F. Caramelo, and G. Veiga, "In vitro zinc-air battery evaluation for use in intraoral medical devices," *Journal of medical devices*, vol. 8, no. 1, 2014. [Online]. Available: https://asmedigitalcollection.asme.org/medicaldevices/article/8/1/014509/376708/In-Vitro-Zinc-Air-Battery-Evaluation-for-Use-in

[21] F. Hussain, M. Z. Rahman, A. N. Sivasengaran, and M. Hasanuzzaman, "Chapter 6 - energy storage technologies," in *Energy for Sustainable Development*, M. Hasanuzzaman and N. A. Rahim, Eds. Academic Press, 2020, pp. 125–165. [Online]. Available: https://www.sciencedirect.com/science/article/pii/B9780128146453000067

[22] G. Ciuti, A. Menciassi, and P. Dario, "Capsule endoscopy: from current achievements to open challenges," *IEEE reviews in biomedical engineering*, 2011. [Online]. Available: https://pubmed.ncbi.nlm.nih.gov/22273791/

[23] R. . S. G. . C. KG, "Near field communication (nfc) technology and measurements," 2013. [Online]. Available: https://www.rohde-schwarz.com/us/applications/near-field-communication-nfc-technology-and-measurements-white-paper_230854-15836.html

[24] A. Abedi, O. Abari, and T. Brecht, "Wi-le: Can wifi replace bluetooth?" in *Proceedings of the 18th ACM Workshop on Hot Topics in Networks*, ser. HotNets

’19. New York, NY, USA: Association for Computing Machinery, 2019, p. 117–124. [Online]. Available: https://doi.org/10.1145/3365609.3365853

[25] Bluetooth Special Interest Group, “Understanding Bluetooth Range,” Online. [Online]. Available: https://www.bluetooth.com/learn-about-bluetooth/key-attributes/range/

[26] M. J. Christoe, J. Yuan, A. Michael, and K. Kalantar-Zadeh, “Bluetooth signal attenuation analysis in human body tissue analogues,” *IEEE Access*, vol. 9, pp. 85 144–85 150, 2021. [Online]. Available: https://ieeexplore.ieee.org/document/9449897

[27] P. Niewiadomy, K. Szuścik-Niewiadomy, M. Rychlik, and K. Piątkowska, “Reliability of the ultrasound measurements of deep abdominal muscle in rehabilitative practice,” *Journal of Orthopaedics Trauma Surgery and Related Research*, vol. 12, 04 2017.

[28] InsightSiP, *ISP2053 Dual-core Bluetooth 5.2 BLE Module with Mesh, NFC, Thread and Zigbee*, 03 2024. [Online]. Available: https://www.insightsip.com/fichiers_insightsip/pdf/ble/ISP2053/isp_ble_DS2053.pdf

[29] ——, *ISP1807 Data Sheet*, 03 2024. [Online]. Available: https://www.insightsip.com/fichiers_insightsip/pdf/ble/ISP1807/isp_ble_DS1807.pdf

[30] Luminus, *Luminus SST-10-Red Product Datasheet*, 2023. [Online]. Available: https://download.luminus.com/datasheets/Luminus_SST-10-R_Datasheet.pdf

[31] Semrock. (n.d.) 628/40 nm brightline® single-band bandpass filter. [Online]. Available: https://www.idex-hs.com/store/product-detail/ff02_628_40_25/fl-004435

[32] ——. (n.d.) 692/40 nm brightline® single-band bandpass filter. [Online]. Available: https://www.idex-hs.com/store/product-detail/ff01_692_40_25/fl-004702?search=true

[33] ams OSRAM Group, *AS7341 11-Channel Multi-Spectral Digital Sensor*, 2020. [Online]. Available: https://look.ams-osram.com/m/24266a3e584de4db/original/AS7341-DS000504.pdf

[34] N. Semiconductor, *nRF5340 Product Specification*, 12 2023. [Online]. Available: https://infocenter.nordicsemi.com/pdf/nRF5340_PS_v1.3.pdf

[35] Molex, *molex 5034801200*, 07 2024. [Online]. Available: https://www.molex.com/en-us/products/part-detail/5034801200?display=pdf

[36] ——, *molex 5050701222*, 08 2024. [Online]. Available: https://www.molex.com/en-us/products/part-detail/5050701222?display=pdf

[37] E. Robledo. (2024, 03) Understanding the power of via stitching in pcb design. [Online]. Available: https://www.autodesk.com/products/fusion-360/blog/understanding-the-power-of-via-stitching-in-pcb-design/

[38] L. Technology. (n.d.) I2c quick guide. [Online]. Available: https://www.analog.com/media/en/technical-documentation/product-selector-card/i2Cb.pdf

[39] N. Semiconductor. (2023, 03) Device power management. [Online]. Available: https://docs.nordicsemi.com/bundle/ncs-2.1.4/page/zephyr/services/pm/device.html

[40] EdmundOptics. (n.d.) 0.98" x 0.98" 0.20" focal length, fresnel lens. [Online]. Available: https://www.edmundoptics.com/p/098-x-098-020-focal-length-fresnel-lens/42289/

[41] ThorLabs. (2013) Frp125 - Ø1" fresnel lens, f = 25 mm. [Online]. Available: https://www.thorlabs.com/thorproduct.cfm?partnumber=FRP125

[42] I. Health and Science. (n.d.) Brightline® single-band filter set, optimized for cy5 and other like fluorophores. [Online]. Available: https://www.idex-hs.com/store/product-detail/cy5_4040c_000/s-000701?cat_id=semrock_optical_filters&node=optical_filter_sets

[43] Carbon, *UMA90*, 2022. [Online]. Available: https://docs.carbon3d.com/files/technical-data-sheets/tds_carbon_uma-90.pdf

[44] Henkel. (n.d.) Loctite® 4902. [Online]. Available: https://next.henkel-adhesives.com/us/en/products/industrial-adhesives/central-pdp.html/loctite-4902/Loctite4902.html

List of Figures

List of Listings

List of Tables

List of Acronyms

ISF Interstitial Fluid

FAD Flavin Adenine Dinucleotide

ASIC Application-Specific Integrated Circuit

IMT Implantable Molecular Tracker

NFC Near Field Communication

BLE Bluetooth Low Energy

LTE Long Term Evolution

MCU Microcontroller Unit

PCB Printed Circuit Board

SDK Software Development Kit

I2C Inter-Integrated Circuit

IC Integrated Circuit

SCL Serial Clock Line

SDA Serial Data Line

GPIO General-Purpose Input/Output

LDO Low Drop Out

LOD Limit of Detection

LOQ Limit of Quantification

SELEX Systematic Evolution of Ligands by EXponential enrichment

DI Deionized

A. Setup

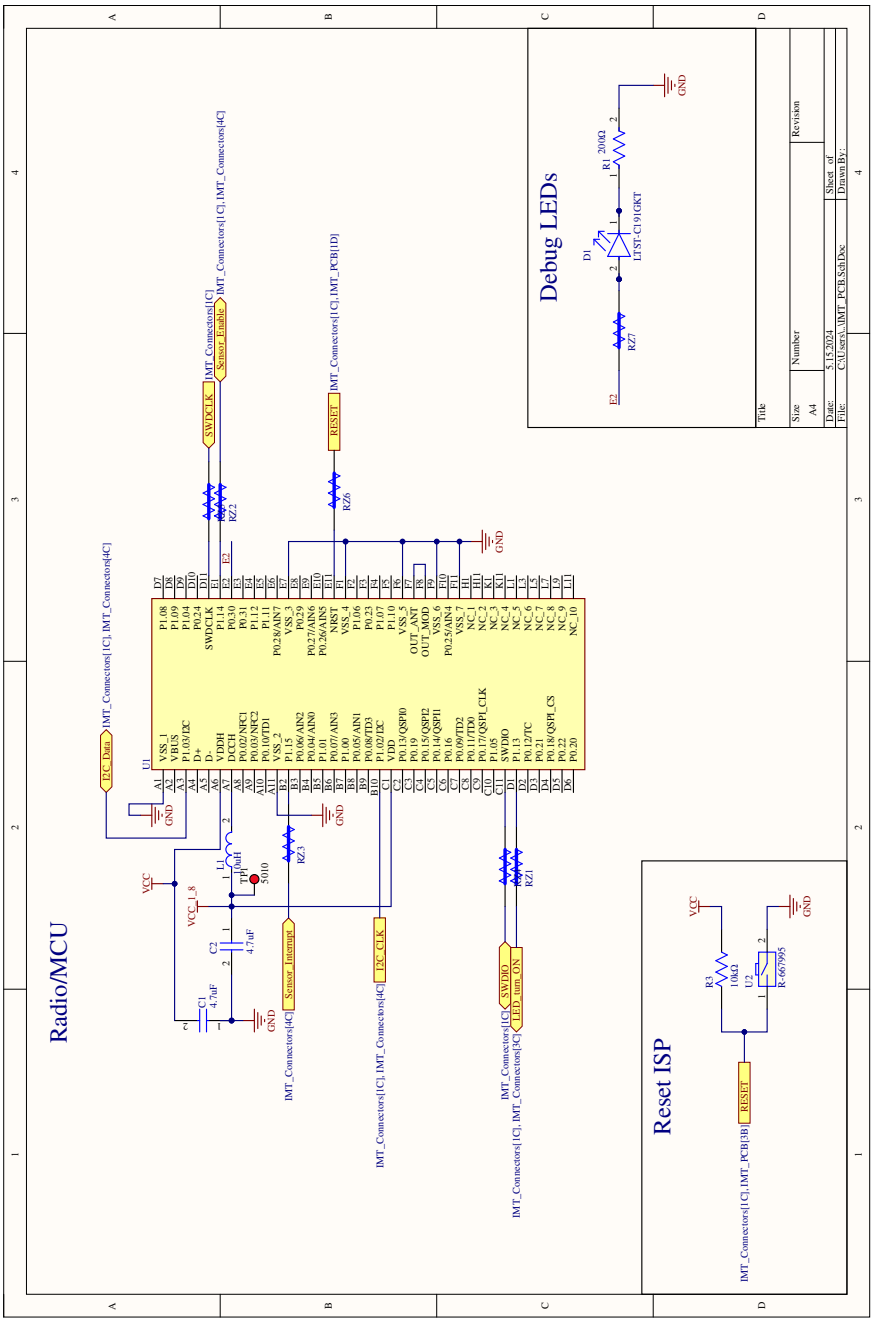

Figure A.1.: First page of the radio PCB schematic overview.

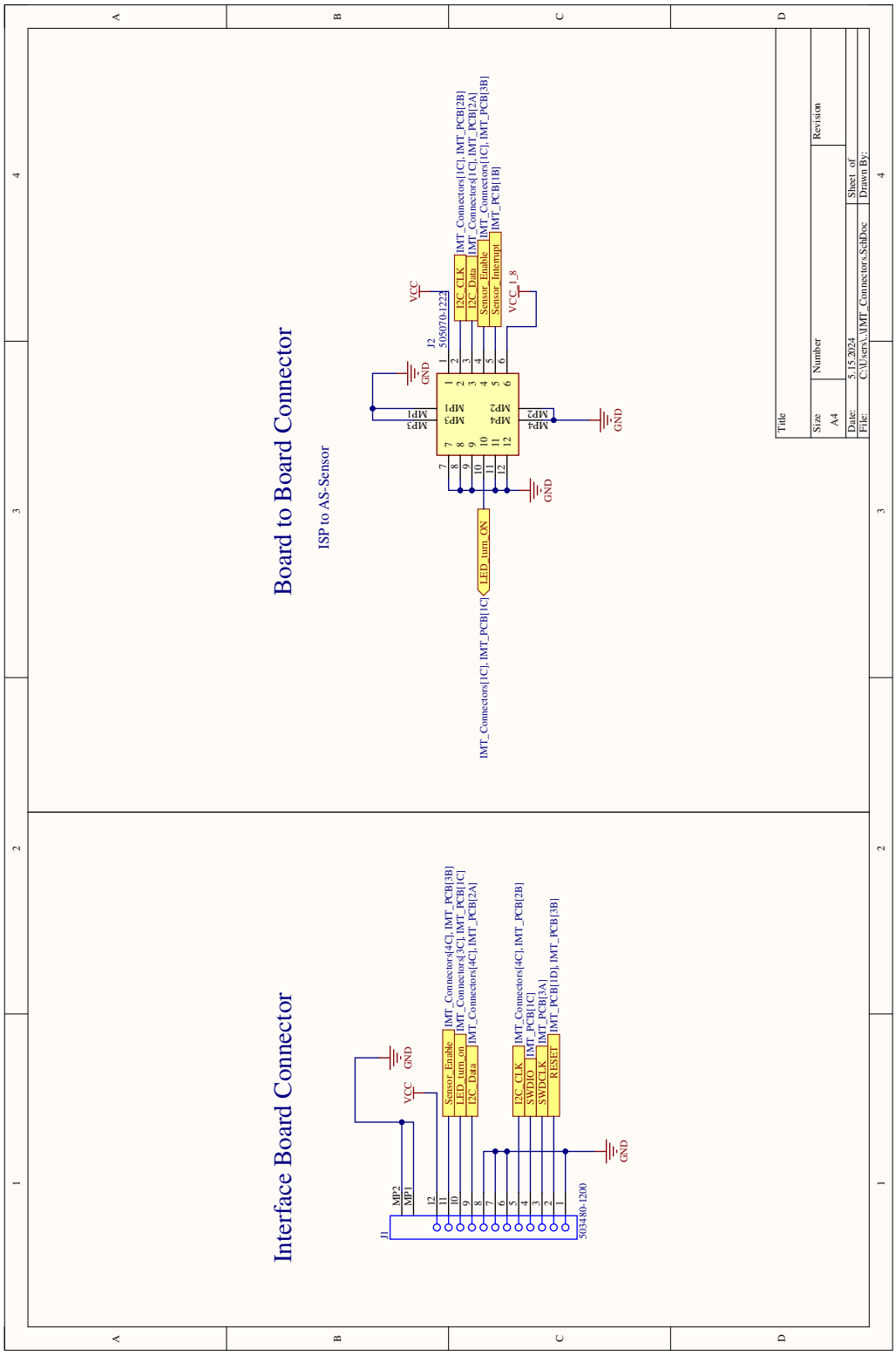

Figure A.2.: Second page of the radio PCB schematic overview.

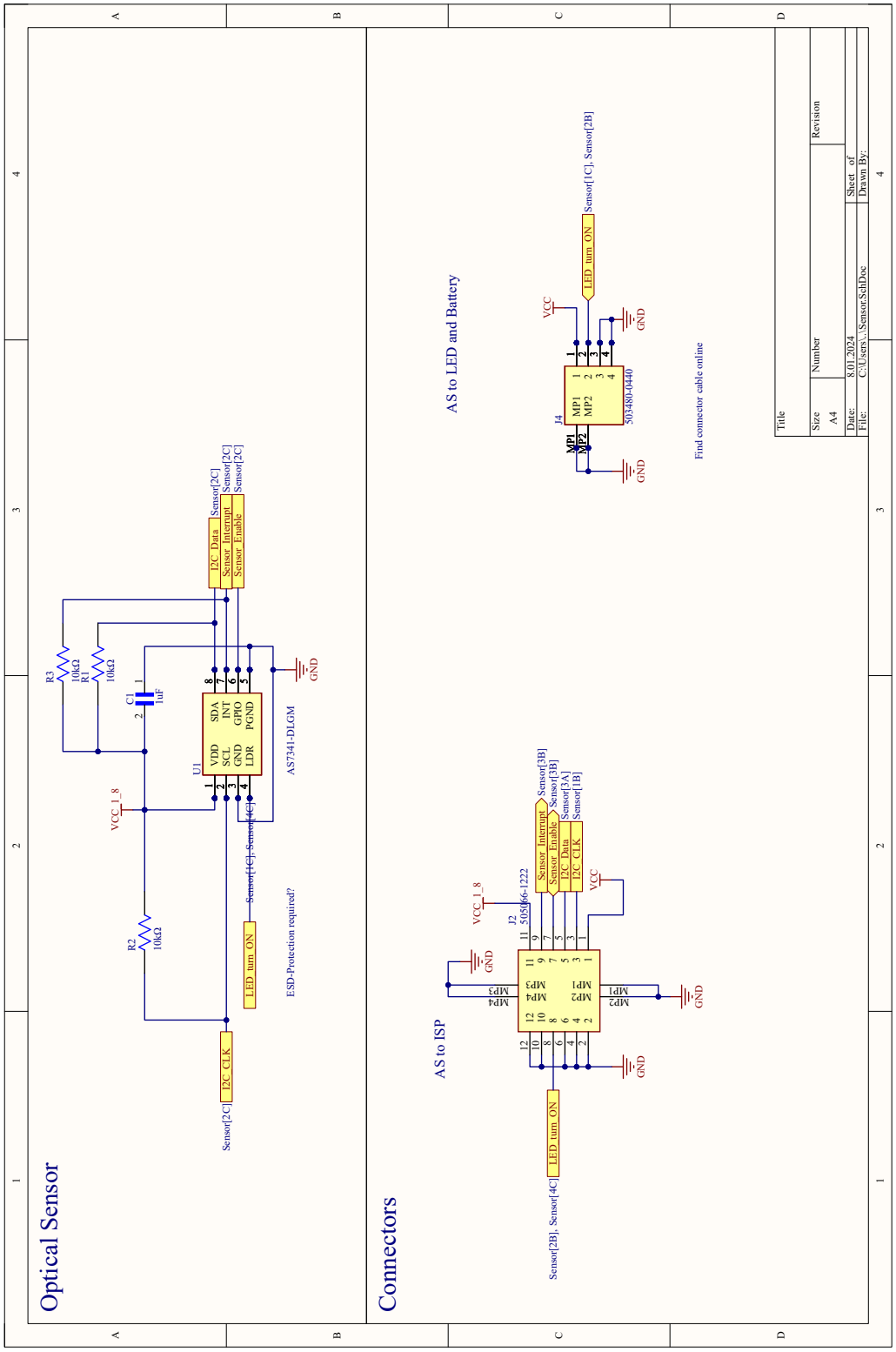

Figure A.3.: Sensor PCB schematic overview.

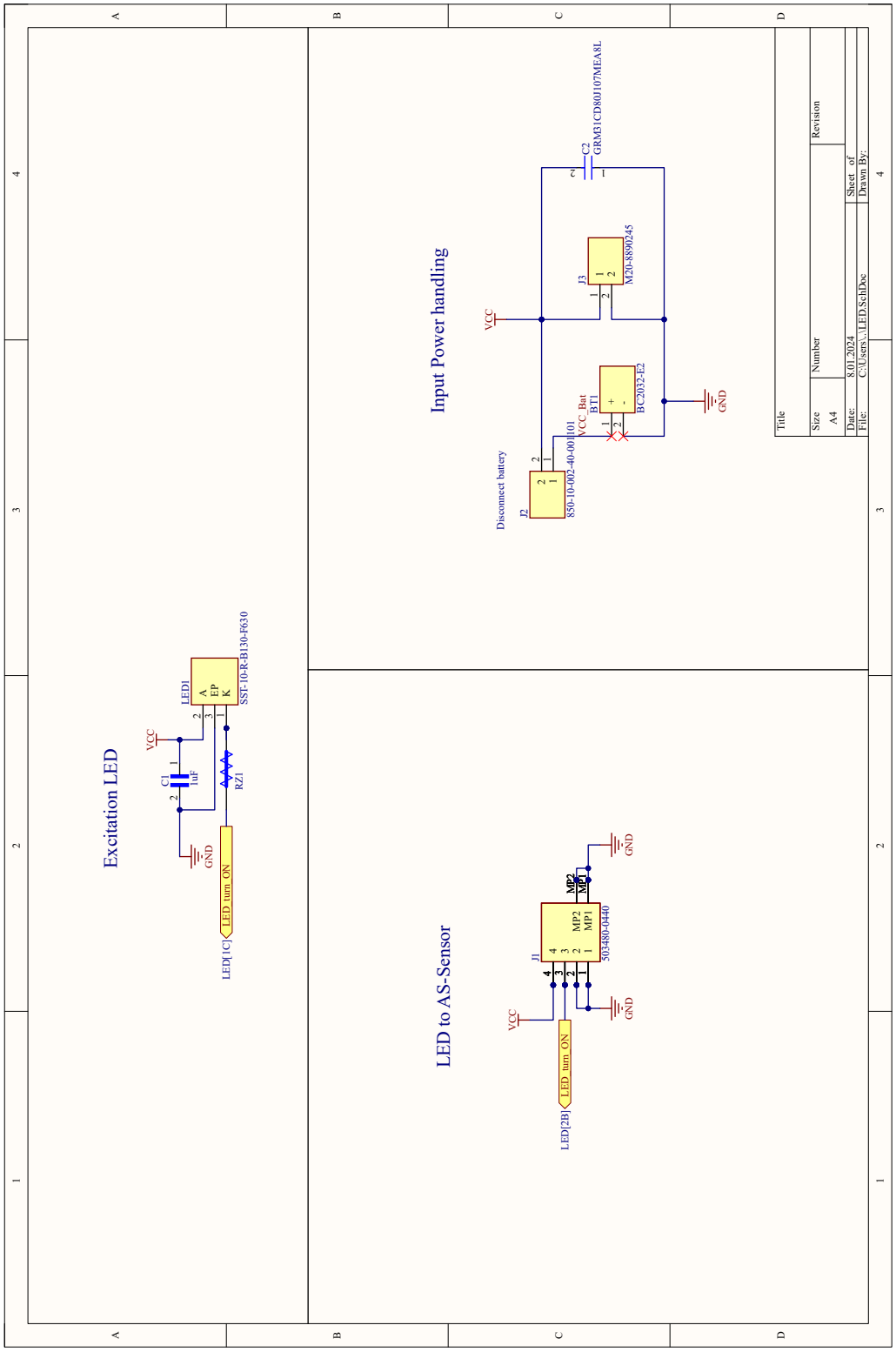

Figure A.4.: LED PCB schematic overview.

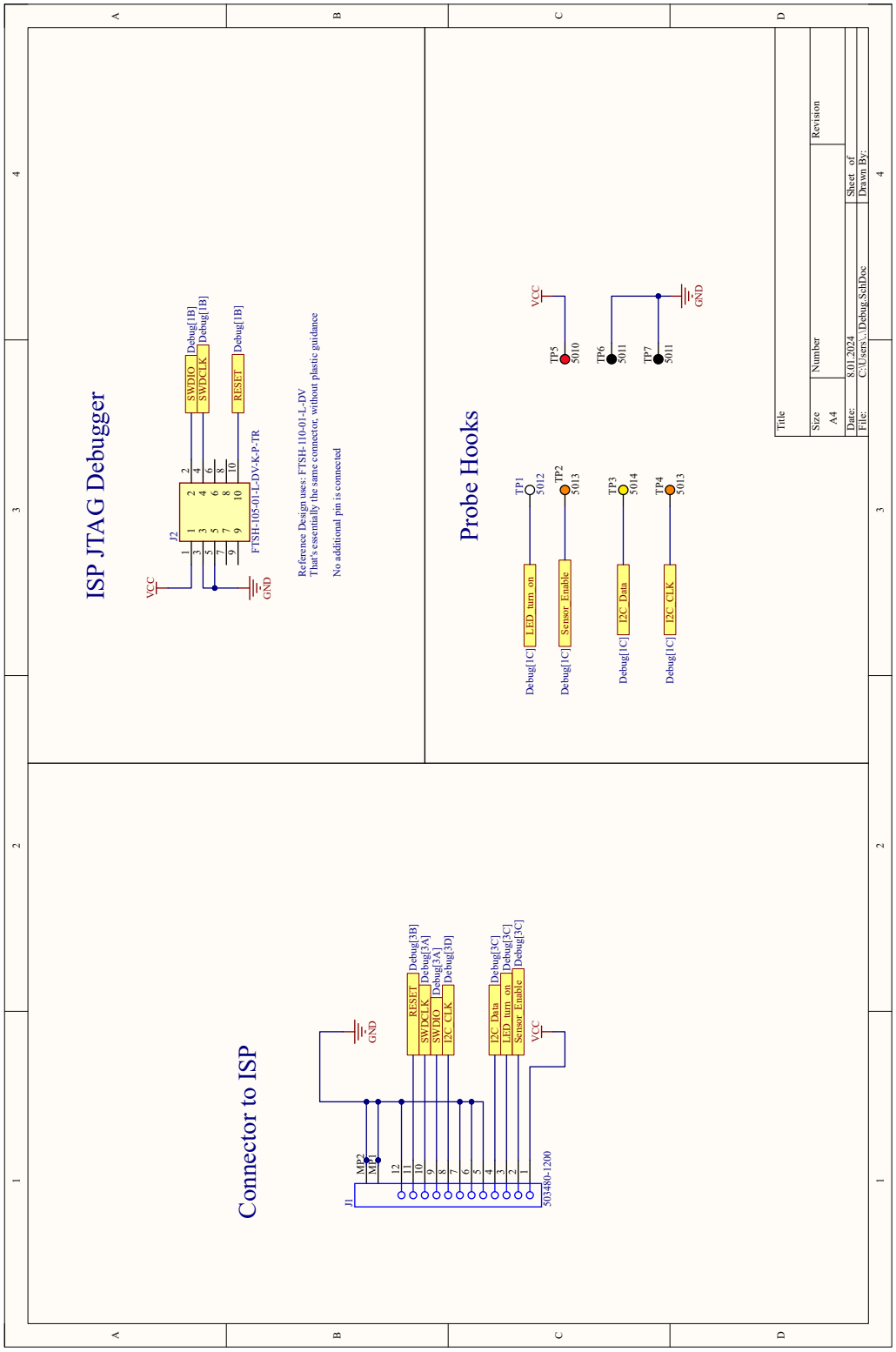

Figure A.5.: Debug PCB schematic overview.